RXTE Monitoring of the Anomalous X-ray Pulsar 1E 1048.1−5937: Long-Term Variability and the 2007 March Event

Rim Dib[1], Victoria M. Kaspi[1], and Fotis P. Gavriil[2,3]

ABSTRACT

After three years of no unusual activity, Anomalous X-ray Pulsar 1E 1048.1−5937 reactivated in 2007 March. We report on the detection of a large glitch ($\Delta\nu/\nu = 1.63(2) \times 10^{-5}$) on 2007 March 26 (MJD 54185.9), contemporaneous with the onset of a pulsed-flux flare, the third flare observed from this source in 10 years of monitoring with the *Rossi X-ray Timing Explorer*. Additionally, we report on a detailed study of the evolution of the timing properties, the pulsed flux, and the pulse profile of this source as measured by *RXTE* from 1996 July to 2008 January. In our timing study, we attempted phase coherent timing of all available observations. We show that in 2001, a timing anomaly of uncertain nature occurred near the rise of the first pulsed flux flare; we show that a likely glitch ($\Delta\nu/\nu = 2.91(9) \times 10^{-6}$) occurred in 2002, near the rise of the second flare, and we present a detailed description of the variations in the spin-down. In our pulsed flux study, we compare the decays of the three flares and discuss changes in the hardness ratio. In our pulse profile study, we show that the profile exhibited large variations near the peak of the first two flares, and several small short-term profile variations during the most recent flare. Finally, we report on the discovery of a small burst 27 days after the peak of the last flare, the fourth burst discovered from this source. We discuss the relationships between the observed properties in the framework of the magnetar model.

Subject headings: pulsars: individual(1E 1048.1−5937) — stars: neutron — X-rays: stars

1. Introduction

The source 1E 1048.1−5937 is part of the class of sources known as Anomalous X-ray Pulsars (AXPs). They have generally been characterized by a persistent X-ray luminosity in excess of available spin-down power, although there are exceptions (e.g. AXP 1E 1547.0−5408 in 2006 (Camilo et al. 2007; Gelfand & Gaensler 2007)). AXPs are young, isolated pulsars with a large inferred magnetic field ($> 10^{14}$ G). They are detected across the electromagnetic spectrum from the radio (in 2 cases) to the hard X-ray regime. Just like a closely related class of pulsars, the Soft Gamma Repeaters (SGRs), AXPs exhibit a wide range of variability, including but not limited to spectral variability, timing glitches, X-ray bursts, X-ray pulsed and persistent flux "flares", and pulse profile changes. For recent reviews, see Kaspi (2007) and Mereghetti (2008).

The magnetar model (Thompson & Duncan 1995; Thompson & Duncan 1996; Thompson et al. 2002) recognizes the power source of these objects to be the decay of their strong magnetic fields. In this model, the bursts of high-energy emission are thought to occur when the crust succumbs to the internal magnetic stresses and deforms. The deformation twists the footpoints of the external magnetic field, driving currents into the magnetosphere and twisting it relative

[1]Department of Physics, McGill University, Montreal, QC H3A 2T8

[2]Center for Research and Exploration in Space Science and Technology, NASA Goddard Space Flight Center, Code 662, Greenbelt, MD 20771, USA.

[3]Department of Physics, University of Maryland Baltimore County, 1000 Hilltop Circle, Baltimore, MD 21250, USA.

to the standard dipolar geometry. These magnetospheric currents resonantly cyclotron-scatter seed surface thermal photons, giving rise to the non-thermal component of the spectrum, usually fitted to a power-law model below 10 keV. Additionally, the high energy X-ray spectrum of magnetars may be explained by the existence of a plasma corona contained within the closed magnetosphere (Beloborodov & Thompson 2007).

We have been monitoring 1E 1048.1−5937 with the *Rossi X-ray Timing Explorer* (*RXTE*) since 1997. During that time, the AXP has exhibited significant timing and pulsed flux variability. Early regular monitoring showed that the spin-down of 1E 1048.1−5937 was so unstable that phase coherence could be maintained for periods of only a few months at a time (Kaspi et al. 2001). In late 2001, two small bursts were detected from this AXP (Gavriil et al. 2002). The first of the two bursts coincided with the rise of the first of two consecutive slow pulsed flux flares (Gavriil & Kaspi 2004). The second flare, the longer-lasting of the two, decayed during the second half of 2002, and throughout 2003 and 2004. A third burst was observed from the source during this decay (Gavriil et al. 2006). While the second pulsed flux flare was ongoing, Mereghetti et al. (2004) and Tiengo et al. (2005) reported an enhancement in the total flux of the source followed by a decay based on data from X-ray imaging observations. The source was also seen to brighten in the IR at the onset of the second flare (Wang & Chakrabarty 2002; Israel et al. 2002).

In 2003, during the decay of the second flare, Gavriil & Kaspi (2004) reported order-of-magnitude variations in the spin-down of the pulsar on timescales of weeks to months. In 2004, near the end of the decay of the second flare, the source entered a quiescent period in which the pulsed flux slowly decreased, with much smaller and more monotonic variations in the spin-down. Then, in 2007 March, the source entered a new active phase. Dib et al. (2007b) reported the detection of a sudden spin-up accompanied by pulsed flux increase (hereafter referred to as the third flare) in regular *RXTE* monitoring data. The enhancement in the phase-averaged X-ray and infrared fluxes that accompanied this new flare are discussed in detail in Tam et al. (2008). Wang et al. (2008) reported on an optical enhancement, and very recently Dhillon et al. (2009) have reported contemporaneous optical pulsations.

Here we present a detailed analysis of all *RXTE* observations of 1E 1048.1−5937 that were taken between 1996 July 03 and 2008 January 09. We report the results of an in-depth analysis of the timing behavior, pulsed flux changes, and pulse profile variations. These results include but are not limited to those obtained from the analysis of the 2007 March events. We also report on the detection of a fourth small burst on 2007 April 28. Our observations are described in Section 2. Our timing, pulsed morphology, and pulsed flux analyses are presented, respectively, in Sections 3, 4, and 5. In Section 6, we discuss the most recent burst. Finally, in Section 7, we compare the observed properties of 1E 1048.1−5937 to those of the other AXPs, and we discuss the implications of our findings in the framework of the magnetar model.

2. Observations

The results presented here were obtained using the proportional counter array (PCA) on board *RXTE*. The PCA consists of an array of five collimated xenon/methane multi-anode proportional counter units (PCUs) operating in the 2−60 keV range, with a total effective area of approximately 6500 cm^2 and a field of view of $\sim 1^\circ$ FWHM (Jahoda et al. 1996).

There are 841 *RXTE* observations of 1E 1048.1−5937 taken between MJD 50294.3 (1996 July 03) and MJD 54474.7 (2008 January 09). We used 821 of them for the analysis presented in this paper. The remaining observations were excluded for various reasons (unusually short observations, pointing errors, or missing files).

The length of the observations varied between 0.75 ks and 45 ks, but most of them were 2 ks long (see Figure 1). The time intervals between the observations are shown in Figure 2. The observation frequency varied over the years from once per month to several times per month. Because it was difficult to achieve long-term phase-coherent timing for this source (Gavriil & Kaspi 2004), in 2002 March, we adopted the strategy of observing it three times every two weeks with three closely

spaced observations. The bold vertical line in Figures 1 and 2 mark when this strategy was implemented. The observing frequency increased to three times per week in 2005 March.

Throughout the monitoring, we used the `GoodXenonwithPropane` data mode to observe this source, except during *RXTE* Cycles 10 and 11 when we used the `GoodXenon` mode. Both data modes record photon arrival times with 1-μs resolution and bin photon energies into one of 256 channels. To maximize the signal-to-noise ratio, we analysed only those events from the top Xenon layer of each PCU.

3. Phase-Coherent Timing Study: Analysis and Results

3.1. Long-Term Timing

To do the timing analysis, photon arrival times at each epoch were adjusted to the solar system barycenter. Resulting arrival times were binned with 31.25-ms time resolution. In the timing timing analysis, we included only events in the energy range 2−5.5 keV, to maximize the signal-to-noise ratio of the pulse. Each barycentric binned time series was epoch-folded using an ephemeris determined iteratively by maintaining phase coherence as we describe below. When an ephemeris was not available, we folded the time series using a frequency obtained from a periodogram. Resulting pulse profiles, with 64 phase bins, were cross-correlated in the Fourier domain with a high signal-to-noise template created by adding phase-aligned profiles. The cross-correlation returned an average pulse time of arrival (TOA) for each observation corresponding to a fixed pulse phase. The pulse phase ϕ at any time t can usually be expressed as a Taylor expansion,

$$\phi(t) = \phi_0(t_0)+\nu_0(t-t_0)+\frac{1}{2}\dot{\nu_0}(t-t_0)^2+\frac{1}{6}\ddot{\nu_0}(t-t_0)^3+\ldots, \quad (1)$$

where $\nu \equiv 1/P$ is the pulse frequency, $\dot{\nu} \equiv d\nu/dt$, etc., and subscript "0" denotes a parameter evaluated at the reference epoch $t = t_0$.

To obtain ephemerides for data prior to 2001, we fitted the TOAs to the above polynomial using the pulsar timing software package `TEMPO`[1]. `TEMPO` also returned an absolute pulse number associated with each TOA, corresponding to the number of times that the pulsar rotated since the first TOA. Since the spin-down of this source was unstable, phase coherence could only be maintained for periods of several months at a time (Kaspi et al. 2001).

After 2002 March 02, we started observing 1E 1048.1−5937 using sets of three closely spaced observations. For data after this date, we adopted a new timing strategy. We broke the list of TOAs into several segments. Each segment lasted between 8 and 16 weeks (4 to 8 weeks after 2005 March), with an overlap between one segment and the next of at least four weeks (2 weeks after 2005 March), except for the week of 2003 April 13 (MJD 52742) where the overlap was of two weeks only, and except at the onset of the flares where there was no overlap. For each two overlapping segments, we used `TEMPO` to fit the TOAs with Equation 1 and extract pulse numbers. We then checked that the pulse numbers of the observations present in both segments were the same. This gave us confidence that the two overlapping ephemerides were consistent with each other and that phase coherence was not lost. Combining all overlapping segments between two given dates yielded a time series of absolute pulse number versus TOA. The errors on the TOAs were converted into fractional errors on the pulse numbers. We also used `TEMPO` to fit the TOAs obtained between 2001 and 2002 March 02 with two non-overlapping ephemerides and extracted pulse numbers.

All the pulse numbers obtained using the procedure above were then organized into four different pulse number versus TOA time series: a time series covering the time interval between 2001 and the onset of the first flare (2001 March to 2001 October), a time series covering the interval between the onset of the first flare and that of the second (2001 November to 2002 April), a time series covering the interval between the onset of the second flare and that of the third (2002 May to 2007 March), and a time series covering the interval between the onset of the third flare and the date of the last observation included in this paper (2007 March to 2008 January).

Because of the instability of the spin-down of AXP 1E 1048.1−5937, timing solutions spanning long periods of time required the use of very high-order polynomials which tended to oscillate at the

[1]See http://www.atnf.csiro.au/research/pulsar/tempo.

end points of fitted intervals. Instead of using these polynomials, we used splines. A spline is a piecewise polynomial function. It consists of polynomial pieces of degree n (here $n = 5$) defined between points called knots. The two polynomial pieces adjacent to any knot share a common value and common derivative values at the knot, through the derivative of order $n-2$ (see Dierckx, 1975 for more details about splines). We fit a spline function through each of the above time series, weighted by the inverse of the square of the fractional errors on the pulse numbers. To minimize oscillations in the spline due to noise, we set the spline smoothing parameter to allow the RMS phase residual obtained after subtracting the spline from the data points to be twice the average 1σ uncertainty in the pulse phase. The smoothing parameter controls the tradeoff between closeness and smoothness of fit by varying the polynomial coefficients and the spacing between the knots. We found the uncertainties on the spline by adding Gaussian noise to our data points 500 times, with mean equal to the 1σ uncertainty on each data point, fitting each time with a spline, averaging all the splines, and finding the standard deviation at each point.

The derivative of the spline function is the frequency of the pulsar, and the second derivative of the spline function is the frequency derivative of the pulsar.

The results of this timing analysis are presented in Figure 3. The top panel of Figure 3 shows frequency versus time. The first horizontal double arrow indicates a time interval in which 1E 1048.1−5937 was not observed with *RXTE*. The second horizontal arrow indicates a time interval in which data were so sparse that multiple phase-coherent timing solutions could be found. The first two plotted curves are ephemerides obtained using `TEMPO` only. They are consistent with the first three ephemerides reported in Kaspi et al. (2001). The remaining plotted curves are ephemerides obtained from taking the derivatives of spline functions. The slope of the diagonal dotted line is the average spin-down of the pulsar. The deviations from the average spin-down are clear to the eye. Note that since the onsets of the first two flares were accompanied by significant pulse profile changes, we did not include the data from the two weeks surrounding each in this Figure (see Sections 3.2, and 3.3).

The second panel of Figure 3 shows the timing residuals for all phase-connected intervals. The RMS residuals for the two intervals fitted with `TEMPO` are 2.4% and 1.9% of a pulse cycle. The RMS residuals for the four intervals fitted with splines are 3.2%, 3.5%, 1.2%, and 2.1% of the pulse cycle. The slow increase in the values of the uncertainties between 2004 and the onset of the third flare reflects a decrease in signal-to-noise that is due both to a decrease in the pulsed flux of the source and to a decrease in the effective number of operational PCUs onboard *RXTE*. The uncertainties are smaller after the flare due to the rise in the pulsed flux.

The third panel of Figure 3 shows the frequency versus time after having subtracted the long-term average linear trend shown in the top panel. The two early ephemerides were obtained with `TEMPO`. The curves, representing the remaining ephemerides, were obtained from derivatives of splines. The points marked as squares are the values of the derivative evaluated at the epochs at which observations were taken. A detailed timing analysis of data inside the circles is done in Sections 3.2, 3.3, and 3.4.

We note in this panel that the spin-down of the pulsar was significantly enhanced starting a few months after the onset of the second flare, a phenomenon which lasted until 2004. In this period of time the pulsar's rotational evolution became much noisier and phase-coherent timing would not have been possible without the availability of sets of three closely spaced observations. Note that Gavriil & Kaspi (2004) previously reported this phenomenon without using long-term phase-coherent timing: they obtained individual frequency measurements by finding the frequency that best fit each three observations.

In the same panel, we can also see that the pulsar then entered a quiescent period in mid-2004 during which the frequency evolution was closer to the long-term average. Note that even though the frequency evolution in the pre-2000 and post-2004 years looks stable, an analysis performed by Archibald et al. (2008) of 1E 1048.1−5937 data between 2004 and 2007 reveals that the amplitude of the timing noise (deviations from a simple spin-down) of this AXP is significantly larger than that seen thus far for any other AXP.

Finally, in 2007 March, the pulsar underwent one of the largest glitches yet observed in an AXP. The frequency jump inside the third circle is clear to the eye. This is discussed in detail in Section 3.4.

The fourth panel of Figure 3 shows the frequency derivative versus time. The first two plotted curves are obtained with `TEMPO`. The remaining four curves, spanning data from 2001 to 2008, and separated by the solid lines that mark the onset of the three flares, are obtained by taking the second derivative of spline functions. The points marked as squares are the values of that derivative evaluated at the epochs where observations were taken. Note that the large error bars at the beginning and end of each curve reflect the fact that the extremes of the curves are not well constrained by the data.

We note in this panel that, starting a few months after the onset of the second flare, the pulsar underwent frequent and significant variations in its spin-down on timescales of weeks to months. The variations noted in this plot are consistent with those reported by Gavriil & Kaspi (2004) although our analysis here has higher time resolution. This is because in that study, the spin-down was determined in short intervals by calculating the slope of three consecutive frequency measurements, and each frequency measurement was obtained by phase-connecting a group of three closely spaced observations.

More specifically, we note that $\dot{\nu}$ was stable from 29 days preceding the peak of the second flare, until 41 days following the flare, fluctuating around the value $\sim -2.3\times10^{-13}$ s^{-2} with variations on the order of 0.08×10^{-13} s^{-2} every two weeks. Then, from the 41 days to 141 days after the flare, $\dot{\nu}$ dropped an average of 2×10^{-13} s^{-2} every two weeks. The very rapid changes in $\dot{\nu}$ started 141 days after the peak of the flare. From 141 to 196 days after the flare, $\dot{\nu}$ dropped an average of 5.6×10^{-13} s^{-2} every two weeks. $\dot{\nu}$ then fluctuated between -26×10^{-13} s^{-2} and -6×10^{-13} s^{-2} 4 times in the space of 450 days. During this period of unusual activity, there are four significant upward jumps in $\dot{\nu}$. Although none of the measured peak values of $\dot{\nu}$ is positive, spin-up glitches could still have occurred between measurements.

This panel also shows that the frequency derivative stabilized between 2004 and 2007. It then appears to have decreased before the large glitch associated with the third flare. However, this decrease stops in the two weeks preceding the flare (see Section 3.4).

After the glitch, $\dot{\nu}$ increased by $\sim 0.33\times10^{-13}$ s^{-2} every week, rising from $\sim -7.7\times10^{-13}$ s^{-2} to -2.9×10^{-13} s^{-2} in $\sim$130 days before starting to fall continuously again at the same rate. A preliminary analysis of the most-recent data shows that in 2008 May, the pulsar appears to have entered a new noisy phase (not shown in the Figure). Weekly variations in $\dot{\nu}$ starting roughly a year after the onset of the third flare are similar to, but a factor of $\sim$2 smaller, than the variations observed starting 141 days after the peak of the second flare. This noisy phase was still ongoing as of 2008 November 17.

3.2. Timing Around the First Flare

In this Section we describe the analysis of the TOAs in the 14 weeks surrounding the onset of the first flare (MJD 52254 − 52163). We show here that a previously unreported and puzzling timing anomaly occured and was coincident with the rise of the flare. The results are presented in Figure 4.

In panel a, two lines, representing two ephemerides, are plotted. The left ephemeris is obtained by fitting a frequency and a frequency derivative through the pre-flare data, excluding the data between the dotted lines. The right ephemeris is obtained by fitting the same parameters through the post-flare data, again excluding the data between the dotted lines. If we extend both ephemerides toward each other, it appears that a spin-up glitch of size $\Delta\nu \sim 1 \times 10^{-7}$ s^{-1} occured near the onset of the flare. The residuals obtained from the two fits are presented in panel b.

In Section 4, we show that the pulsar underwent pulse profile changes near the onset of the flares. Because we could not be certain that our TOAs, obtained by cross-correlating the profiles of the individual observations with a long-term template, were not affected by pulse profile changes, we created two additional sets of TOAs. The first additional set was obtained by aligning the tallest peak in the each profile with the tallest peak in the template, and extracting a phase offset The second additional set was obtained by aligning the

lowest point in each profile with the lowest point in the template.

In panel c, we subtracted all three sets of TOAs from the pre-flare ephemeris and plotted the residuals. The points marked with solid circles represent the residuals obtained from the original set of TOAs. The points marked with empty circles and empty triangles represent the residuals obtained from the two additional sets of TOAs. While the scatter in the residuals corresponding to the additional sets of TOAs is large, note how all three sets of residuals follow the same trend, indicating that it is unlikely to be caused by pulse profile changes. However, it cannot be ruled out that the trend is caused by the motion of the active region. The difference in phase between each solid circle and the corresponding empty circle and empty triangle represents our uncertainty in determining a fiducial point on the pulsar. Also note that subtracting a full phase turn from all post-flare residuals, which would yield a different timing solution, would require a non-zero phase jump to have occured near the onset of the flare, which would imply an unphysically large torque on the star.

Assuming the pulse numbers on which the residuals in panel c are based are correct, we fit the pulse arrival times from the 14 weeks surrounding the start of the flare with a spline. The spline subtracted from the pre-flare ephemeris is the curve shown in panel c. The residuals after subtracting the TOAs from the spline are shown in panel d. These residuals are clearly not featureless.

The first derivative of the obtained spline, which is the frequency of the pulsar, is shown in panel e. Notice the anomalous "dip" in frequency surrounding the onset of the flare. The rapidly changing frequency derivative is shown in panel f. The rms pulsed flux is shown for reference in panel g (see Section 5 for more details on how the pulsed flux is calculated). Notice how the dip in the frequency of the pulsar started before the rise in the pulsed flux.

To summarize, a timing anomaly occured near the onset of the first flare. Careful analysis shows that it is not consistent with a simple spin-up glitch, but with a gradual slow down lasting 2−3 weeks, followed by a recovery. The rotational event appears to have preceded the flux event.

3.3. Timing Around the Second Flare

In this Section we describe our analysis of the TOAs in the 28 weeks surrounding the onset of the second flare (MJD 52282 − 52485). We have discovered that a likely spin-up glitch occured during the week when the pulsed flux started rising. We found this glitch while we were trying to fit all available data with short simple overlapping ephemerides and encountered a discontinuity. The results are presented in Figure 5.

Once again, because of pulse profile changes around the start of the flare, we generated two additional sets of TOAs by correlating the highest and lowest points of the individual pulse profiles with the long-term template and extracting phase differences. The residuals after subtracting all three sets of TOAs from the pre-flare ephemeris are shown in panel a of Figure 5. Once again, the scatter in the residuals obtained from the additional sets of TOAs is larger than that obtained from the standard TOAs, but all three sets follow the same trend.

The trend in the residuals shown in panel a indicates that a glitch occured. However, due to the finite resolution of the data (sets of three closely-spaced observations obtained every two weeks, starting in 2002 March), which is particularly problematic given the extreme timing noise of this source, a rapid non-instantaneous variation cannot be ruled out. The curvature following the glitch is due to a change in the frequency derivative rather than glitch recovery. Because the largest pulse profile changes occured in the week the pulsed flux started rising (see Section 5), there is large scatter in the three standard TOAs obtained then. Because of this scatter, it was not possible to determine if the glitch occured before or after the pulsed flux started to rise. The glitch epoch was MJD 52386.0 ± 1.5. The dates of the first three observations having a larger pulsed flux than the pre-flare long-term average are MJD 52385.5, 52386.6, and 52386.7. The change in the frequency at the time of the glitch was $\Delta\nu = 4.51(14) \times 10^{-7}$ s^{-1} ($\Delta\nu/\nu = 2.91(9) \times 10^{-6}$). The change in frequency derivative was $\Delta\dot{\nu} = -4.10(15) \times 10^{-14}$ s^{-2}.

The pre-flare and post-flare ephemerides are shown in panel b of Figure 5. Note the difference in slope between them. The residuals are shown in panel c. The pulsed flux is shown for reference

in panel d. Each pulsed flux data point is the average of the pulsed flux values obtained from three closely spaced onservations.

To summarize, a glitch, or a very rapid change in the frequency, as well as a significant change in the frequency derivative, occured during the week the second pulsed flux flare started rising. Because of the large uncertainty on the glitch epoch, which is due to the pulse profile changes near the onset of the flare, it is not possible to determine which happened first, the rise in the pulsed flux, or the frequency jump.

3.4. Timing Around the Third Flare

In this Section we report on our analysis of the TOAs in the 14 weeks surrounding the onset of the third flare (MJD 54131 − 54223). We show that a large spin-up glitch occured coincident with the rise of the pulsed flux. The results are presented in Figure 6.

We first plotted the pre-flare and post-flare ephemerides in panel a. The pre-flare ephemeris consists of a frequency and three frequency derivatives. The post-flare ephemeris consists of a frequency and a single frequency derivative. The residuals are shown in panel b. Note how in panel a, the pre-flare curve appears to flatten in the two weeks preceding the glitch, indicating that the frequency derivative was becoming less negative. This argues that it is important to choose data as close to the glitch as possible when fitting for the glitch parameters.

In panel c, we show the pre-glitch and the post-glitch timing residuals after subtracting the TOAs from an ephemeris that includes the frequency and frequency derivative that best fit the pre-glitch data. The observed trend in the residuals clearly indicates that a large glitch occured. To obtain the glitch parameters, we performed two different fits with `TEMPO`.

For the first fit, we included data from the 14 weeks surrounding the glitch epoch. We subtracted the TOAs from an ephemeris consisting of the best-fit ν, $\dot{\nu}$, and discrete jump in ν and $\dot{\nu}$ at the glitch epoch. The timing residuals for the first fit are shown in panel d. For the second fit, we included data from the 6 weeks surrounding the glitch epoch. We subtracted the TOAs from an ephemeris consisting of the same set of parameters. The timing residuals for the second fit are shown in panel e. As expected, the best-fit jump in $\dot{\nu}$ at the glitch epoch was significantly larger for the first fit than for the second fit ($1.76(8)\times10^{-13}$ s^{-2} versus $6(4)\times10^{-14}$ s^{-2}). This is because of the rapid change in the frequency derivative in the few weeks preceding the glitch.

From the second fit, the total frequency jump observed at the glitch epoch was $\Delta\nu = 2.52(3) \times 10^{-6}$ s^{-1} ($\Delta\nu/\nu = 1.63(2) \times 10^{-5}$)[2]. The glitch epoch, determined by setting the phase jump to zero at the time of the frequency jump, is MJD 54185.912956 (2007 March 26). For a complete list of the fit parameters, see Table 1.

The pulsed flux is shown for reference in panel f of Figure 6. Each plotted pulsed flux data point is the average of the pulsed flux values obtained from three closely spaced onservations, except in two instances (see Section 5). The date of the last pre-flare observation was MJD 54181.32. The date of the first observation with a large pulsed flux is MJD 54187.67. As explained in Section 5, it is difficult to determine if the pulsed flux of the latter observation is lower than the pulsed flux peak, due to noise. Once again, we cannot determine whether the glitch occured before or after the pulsed flux started rising.

To summarize, a large glitch occured on MJD 54185, two days before the first observation having a large pulsed flux. The change in the frequency derivative at the time of the glitch was not significant, but it was preceded by three weeks where the magnitude of $\dot{\nu}$ was decreasing, which followed a rapid decrease that lasted several weeks. Because of the possibility that the pulsed flux of the first observation after the onset of the flare is consistent with the peak of the flare, we were not able to determine which happened first, the rise in the pulsed flux, or the glitch.

4. Pulse Profile Study: Analysis and Results

Tam et al. (2008) reported pulse profile changes in 1E 1048.1−5937 from imaging data near the third flare. In this Section we confirm their findings and report on additional pulse profile changes

[2]This is different from the value in Dib et al. (2007b) because of a typographical error: the authors reported the value of $\Delta\nu$ instead of reporting the value of $\Delta\nu/\nu$.

near the first two flares.

We performed a first pulse profile analysis using FTOOLS version 5.3.1[3]. Data from PCU 0 were included in the analysis up to 2000 May 12, when it lost its propane layer. Data from PCU 1 were included in the analysis up to 2006 December 25, when it lost its propane layer. We used the procedure described in detail in Dib et al. (2007a) to extract a pulse profile for each observation in the 2−10 keV band. We used 64 phase bins. When a local ephemeris was not available, we folded the data at a pulsar period extracted from a periodogram. We verified that the results of the folding are not very sensitive to the precise period used. We then aligned the 64-bin profiles with a high signal-to-noise template using a cross-correlation procedure similar to that described in Section 3.1.

1E 1048.1−5937 was monitored with *RXTE* from 1997 to 2008. To do the first pulse profile analysis, we divided this time span into many segments, shown with letters at the bottom of Figure 7.

For each time interval, we summed the aligned profiles, subtracted the DC component from the summed profile, and scaled the resulting profile so that the value of the highest bin is unity and the lowest point is zero. The results are presented in Figure 7 with the time intervals marked in the top left corner of each profile. The different profile qualities are due to the segments having different total exposure, and to changes in the pulsed flux of the pulsar.

To look for pulse profile changes on a smaller timescale, we performed a second pulse profile analysis. We extracted a pulse profile for each observation in the 2−10 keV band using all available PCUs to maximize the signal to noise. We used 32 phase bins. We aligned the obtained profiles with the high signal-to-noise template and subtracted the respective average from each of the aligned profiles and from the template. For each observation, we then found the scaling factor that minimized the reduced χ^2 of the difference between the scaled profile and the template. The obtained reduced χ^2 values are plotted in Figure 8.

Figure 7 shows for the first time that the broad pulse profile of 1E 1048.1−5937 developed a small side-peak during the rise and the fall of the first flare (segments d and e). The rise of the second flare (segments g and h) was marked by large profile changes in which the pulse profile was clearly multipeaked. The pulse profile slowly returned to its long-term average shape while the flare was decaying (segments i, j, and k). There were no significant pulse profile changes in the following three years of quiescence (segments l, m, and n), although the profiles in segments m and n seem to have triangular peaks, more so than in segments b, c, and l. Figure 8 confirms the pulse profile changes near the first two flares, and additionally suggests that small occasional profile changes may occur in individual observations throughout segments a, b, c, l, m, and n, but only at the $\sim 2-3\sigma$ level.

It appears from Figure 7 that the pulse profiles in segments o, p, and q, corresponding to the decay of the third flare, were stable and presented no significant deviations from the long-term average on long timescales. However, Figure 8 shows that many significant pulse profile changes occured on short timescales during the decay of the third flare. The changes are clearly visible in the pulse profiles of individual observations having a high signal-to-noise ratio (particularly long observations, or observations with a large numbers of operational PCUs). An example of two such profiles is presented in Figure 9. The top profile is obtained from a 6 ks-long observation taken on 2007 April 09 (14 days after the glitch epoch) with two operational PCUs. The second profile is obtained from a 2 ks-long observation taken on 2007 May 03 (38 days after the glitch epoch). These short-term pulse profile changes are similar to the ones reported in Tam et al. (2008). They were seen mostly in the first two months following the onset of the flare, and occured less often in the next months, although this may be partially due to the reduction in signal-to-noise ratio due to the pulsed flux falling. Several months after the flare small occasional profile changes may be present, but only at the $\sim 2\sigma$ level.

5. Pulsed Flux Study: Analysis and Results

To obtain a pulsed flux time series for 1E 1048.1−5937, for each observation, we created

[3]http://heasarc.gsfc.nasa.gov/ftools

a pulse profile (in units of count rate per PCU) using the same procedure as in Section 4. Data from PCUs 0 and 1 were excluded after the loss of their respective propane layers, because an independent analysis of data from PCU 0 of AXP 4U 0142+61 revealed spectral modeling irregularities after the loss of the propane layer (Dib et al. 2007a). Pulse profiles were generated in three bands: 2−4 keV, 4−10 keV, and 2−10 keV. For each folded profile, we calculated the RMS pulsed flux,

$$F_{RMS} = \sqrt{2\sum_{k=1}^{n}((a_k{}^2 + b_k{}^2) - (\sigma_{a_k}{}^2 + \sigma_{b_k}{}^2))}, \quad (2)$$

where a_k is the $k^{\rm th}$ even Fourier component defined as $a_k = \frac{1}{N}\sum_{i=1}^{N} p_i \cos(2\pi ki/N)$, $\sigma_{a_k}{}^2$ is the variance of a_k, b_k is the odd $k^{\rm th}$ Fourier component defined as $b_k = \frac{1}{N}\sum_{i=1}^{N} p_i \sin(2\pi ki/N)$, $\sigma_{b_k}{}^2$ is the variance of b_k, i refers to the phase bin, N is the total number of phase bins (here N=64), p_i is the count rate in the $i^{\rm th}$ phase bin of the pulse profile, and n is the maximum number of Fourier harmonics used; here n=5.

We verified using an independent pulsed flux estimator calculated from the area under the pulse (i.e. insensitive by definition to ¿ pulse shape) that the trends seen in the RMS pulsed flux of 1E 1048.1−5937 are not a consequence of changes in the pulse profile. The results of the pulsed flux analysis are presented in Figure 10.

In the top panel, we show the pulsed flux results in the 2−10 keV band. For observations taken before 2002 March 02 (date marked with a dashed line), we plotted the pulsed flux values obtained from individual observations. After 2002 March 02, we plotted the average of the pulsed flux values of each set of three closely spaced observations, with the exception of 4 observations. The 4 observations are indicated with arrows located along the bottom of the panel. The first observation, on 2004 June 29, was not averaged with its neighbors because a burst occured within the observation (Gavriil et al. 2006). The second, on 2005 November 08, is an observation with an anomalously high pulsed flux. The third, on 2007 March 28, is the first observation that is part of the most recent pulsed flux flare. The fourth observation, on 2007 April 28, also contained a burst. In each of these cases, we have singled out the abnormal observation, and averaged the other two that were part of the same set. Each of these exceptions is discussed below and in Section 6.

Also in the top panel, the pulsed flux time series obviously has significant structure. The most obvious features are the three long-lived flares. Gavriil & Kaspi (2004) estimated the peak flux of the first flare to occur at MJD 52218.8 ± 4.5, with a risetime of 20.8 ± 4.5 days and a fall time of 98.9 ± 4.5 days. They estimated the peak flux of the second flare to occur at MJD 52444.4 ± 7.0, with a risetime of 58.3 ± 7.0 days and a fall time greater than 586 days. In fact, we can see in the top panel that the second flare continued to decay slowly, and that the pulsed flux had not returned to its pre-flares value by the time the third flare occured. However, the pulsed flux in the year prior to the flares was low compared to the previous years, making it unclear what the real quiescent flux level is.

Here we estimate the peak pulsed flux of the third flare to have occured at MJD 54191.6 ± 3.1, with an upper limit on the risetime of 7.3 days. The three observations obtained in the last week before the flare all had a pulsed flux consistent with quiescence. The three observations obtained 7 days later all had a significantly higher pulsed flux. The first of these three observations, occured 1.75 days after the determined glitch epoch and had a lower pulsed flux than the second observation. The two observations were separated by 22 hours. It is possible that the first observation is part of the rise of the flare, which would imply a resolved rise with a risetime significantly smaller than 7 days. However the value of the pulsed flux for that observation before the binning is less than 3σ away from that of the following observation, and the scatter in the unbinned data near the start of the flare is large. We also estimate the fall time of that flare to be greater than 288 days (date of the last observation included in this paper) since the pulsed flux had not returned to its pre-flare value.

We estimate that the three flares had peak pulsed fluxes of 2.32 ± 0.15, 2.90 ± 0.07, and 3.13 ± 0.10 times the quiescent pulsed flux for the 2−10 keV band. By "quiescent pulsed flux" we mean the average pulsed flux from the year preceding the first flare and from the year preceding

the third flare.

An anti-correlation between the total flux and the pulsed fraction has been reported for this source (Tiengo et al. 2005). Tam et al. (2008) used imaging observations from 1E 1048.1−5937 to derive the following anti-correlation in the 2−10 keV band:

$$F_{tot} = A \times (F_{RMS}/a)^{1/(1+b)}, \qquad (3)$$

where F_{tot} is the total flux of the source in erg/s/cm^2, F_{RMS} is the RMS pulsed flux in counts/s/PCU, a and b are constants (a=1.53, b=−0.46), and A is a constant scaling factor (A∼125). Note that there were no imaging observations obtained in a data mode suitable for extracting pulsed fractions from near the peaks of the first two flares; the parameters in the above equation were obtained on the basis of the third flare only. This information allows us to scale our pulsed fluxes to estimate the total energy released in each flare, assuming that the relation for the third flare holds for the first two as well. Assuming a distance of 2.7 kpc (Gaensler et al. 2005), and assuming roughly linear decays (see Section 7.1), we find a total energy release of $\sim 4.4\times 10^{40}$ erg for the first flare, $\sim 3.1\times 10^{41}$ erg for the second, and $\sim 3.9\times 10^{41}$ erg for the third, all in the 2−10 keV band. For a distance of 9 kpc (Durant & van Kerkwijk 2006), these numbers become $\sim 4.8\times 10^{41}$ erg, $\sim 3.5\times 10^{42}$ erg, and $\sim 4.3\times 10^{42}$ erg.

In the middle panel of Figure 10, we show the pulsed flux results in 2−4 keV (red triangles) and in 4−10 keV (blue squares). Note that in the years between flares 2 and 3 there are two data points with a significantly high pulsed flux in the 4−10 keV band. The corresponding dates are 2004 June 29 (MJD 53185) and 2005 November 08 (MJD 53682). The observation corresponding to the first point contains the third burst detected from this source. Gavriil et al. (2006) reported a pulsed flux increase immediately following the burst, and a slow decay within the 2 ks-long observation (see Section 6). We did not detect a burst within the observation corresponding to the second point, and we found no evidence for a decay in the pulsed flux within the 1.5 ks-long observation. See Section 7.6 for more discussion.

In the bottom panel, we show the ratio of the two pulsed flux time series $H \equiv$ (4−10 keV/2−4 keV). The weighted average hardness ratio for the years preceding the first flare is marked with a magenta horizontal line with $H = 1.04\pm0.02$. The hardness ratios near the peaks of the first two flares are marked with two magenta circles and have $H = 1.6\pm0.1$ and $H = 1.22\pm0.03$, respectively. The hardness ratio for the 4 years preceding the third flare is also marked with a magenta horizontal line with $H = 0.62\pm0.01$. Finally, the hardness ratio after the onset of the third flare is marked with another magenta horizontal line at $H = 0.65\pm0.01$. It is clear from the middle and bottom panels that the pulsed emission from 1E 1048.1−5937 had a harder spectrum near the peaks of the first two flares compared to the pulsed emission preceding the flares. It is also clear that 342 days after the peak of the second flare (first vertical dotted line), this ratio dropped. It dropped again 500 days after the peak of the second flare (second vertical dotted line) to a value smaller than the pre-flares value, a value that was maintained until the onset of the third flare. We verified that these changes in the hardness ratio do not coincide with the epochs of gain change of *RXTE*, nor do they coincide with the dates of loss of the propane layers of PCUs 0 and 1. We also verified that there are no similar changes at the same epochs in the other monitored AXPs.

Note that the hardness ratios reported above are obtained from the pulsed flux of *RXTE*. Any changes in the hardness ratio of the total flux, as observed by an imaging instrument, might not necessarily be reflected in the behavior of the pulsed hardness ratio if the pulsed and persistent spectra are different. Tam et al. (2008) reported an increase in the (3−10 keV)/(1−3 keV) hardness ratio obtained from *Chandra X-ray Observatory* (*CXO*) data at the onset of the third flare. With *RXTE*, we observe a marginal increase in the (4−10 keV)/(2−4 keV) pulsed hardness ratio when we compare the pre-flare and the post-flare data. This can be attributed to the pulsed spectrum having a different evolution from the total phase-averaged spectrum. Indeed we found after analysing data from six *CXO* observations that the dependence of the pulsed fraction on energy is changing with time.

6. A New Burst

Searching for bursts is part of our regular AXP monitoring routine. For each observation of 1E 1048.1−5937, we generated 31.25 ms lightcurves using all Xenon layers and events in the 2–20 keV band. These lightcurves were searched for bursts using the algorithm introduced in Gavriil et al. (2002) and discussed further in Gavriil et al. (2004). Four bursts have been detected from this source. The first two bursts occured on 2001 October 29 and 2001 November 14 (Gavriil et al. 2002). One of these bursts was coincident with the rise of the first pulsed flux flare, and the other with its fall (see Figure 10). The third burst occured on 2004 June 29, 740 days following the peak of the second pulsed flux flare (Gavriil et al. 2004). Here, we report on the detection of a fourth burst[4], which occured on 2008 April 28, 27 days after the peak of the third flare.

6.1. Burst Properties

To analyse the burst, we created event lists in FITS[5] format using the standard `FTOOLS`[6]. For consistency with previous analyses of SGR/AXP bursts, we extracted events in the 2-20 keV band, and reduced them to the solar system barycenter. We subtracted the instrumental background using the model background lightcurve generated by the `FTOOL` `pcabackest`. The model background lightcurve generated by `pcabackest` only has 16-s time resolution. We therefore fit the simulated background lightcurve to a fourth order polynomial and subtracted this model from our high-time-resolution lightcurves. Using the resulting light curve, we then subtracted an additional background determined from a 300-s long interval ending 100-s before the burst. The final background-subtracted burst lightcurve is shown in Figure 11. The burst temporal properties, namely peak time (t_p), peak flux (f_p), rise time (t_r), T_{90}, which is the time from when 5% to 95% of the total burst counts have been collected, and T_{90} fluence were determined using the methods described in Gavriil et al. (2004). The peak flux and T_{90} fluence were then determined in units of erg/s/cm^2 and erg/cm^2, respectively, assuming a power-law spectrum (see below). The burst properties are listed in Table 2. The burst risetime, 955 ms, calculated using a linearly rising model, is longer by a factor of ∼45 than the longest risetime seen from this source to date. The peak flux calculated over a 64-ms time interval (or over the risetime interval) is the lowest of all four bursts. The total burst fluence is within the range of fluences observed for the other bursts from this source.

A burst spectrum was extracted using all the counts above 2 keV within the T_{90} interval. The spectrum was then grouped so as to have at least 20 counts per bin after background subtraction. The bin above ∼40 keV was ignored because it had insufficient counts even after grouping. A response matrix was created using the `FTOOL` `pcarsp`. The burst spectrum, background spectrum, and response matrix were then read into `XSPEC`. The spectrum was fit to a photoelectrically absorbed blackbody and to a photoelectrically absorbed power-law. In both cases, because of *RXTE*'s lack of response below 2 keV, we held the column density fixed to the value found by Tam et al. (2008) ($N_H = 0.97 \times 10^{22}$ cm^{-2}). The power-law model was a poor fit. The blackbody was a better fit but not exceptional, with a 25% probability that the deviations from the model are due to random noise only, given the number of degrees of freedom (see Table 2). Two component-models such as two blackbodies or a blackbody plus power-law did not improve the fits. Two other bursts from this source exhibited spectral features at ∼14 keV. To determine whether the burst exhibited any spectral features that might have been smeared out by extracting a spectrum over the burst's long T_{90} interval, we repeated the above procedure for the first few seconds of the burst. There was indeed excess at ∼ 14 keV when fitting the spectrum of the burst with a simple continuum model (see Fig. 12). To establish the veracity of the feature we performed the following Monte Carlo simulations. We generated 1000 simulated spectra having the same count rate and exposure as our data and a photoelectrically absorbed blackbody shape. The simulated spectrum was created using the kT value found from the best fit line+gaussian model. We then added Poisson

[4]The burst search routine also returned several candidate bursts with a significance several orders of magnitude smaller than those reported for the published bursts. We do not report on the analysis of these putative bursts here.

[5]`http://fits.gsfc.nasa.gov`

[6]`http://heasarc.gsfc.nasa.gov/docs/software/ftools/`

noise to our simulated spectra, fit them with a simple photoelectrically absorbed blackbody model, and calculated a χ^2 value. Next, we added a spectral line to our fitting model and refit the data. To prevent the fit from falling into a local minimum, when doing the fitting, we stepped the central energy of the line from 2 keV to 40 keV in steps of 0.1 keV, but allowed the width and normalization of the line to vary. We found 17 cases out of 1000 for which the addition of a line induced a change in χ^2 that was greater than or equal to that found from adding a line to the model used to fit the real data. Thus, we place a significance of 99.983% on the line which is equivalent to a 2.1-σ detection. This is not a highly significant detection, nor is it as significant as the other lines seen from this source (Gavriil et al. 2002; Gavriil et al. 2006), however, it is highly suggestive that given there have been only four bursts seen from this source, two of which have shown similar features at comparable energies.

6.2. Short-Term Pulsed Flux Variability and Burst Phases

We show the 2−20 keV lightcurves of the 4 seconds surrounding each of the 4 bursts discovered from 1E 1048.1−5937 in the top panels of Figure 13. Each column corresponds to a burst. For each of the observations containing bursts, we made three barycentric time series in count rate per PCU, for the 2−4, 4−20, and 2−20 keV bands. The time resolution was 31.25 ms. We removed the 4 s centered on each burst from each time series. Then, we broke each time series into six segments. For each segment, we calculated the RMS pulsed flux. The results are presented in the middle panels of Figure 13. A similar analysis was performed for burst 3 by Gavriil et al. (2004). Note the significant increase in the 4−20 keV pulsed flux in the observations containing the first, third, and last bursts following the onset of the bursts, while the pulsed flux remained constant in the 2−4 keV band in those same events.

To determine the phase of each burst, we folded each observation at the best-fit frequency and found when, relative to the folded profile, the burst peak occured. We then aligned each of the folded profiles with a high signal-to-noise long-term average profile. The pulse phases are shown in the bottom panels of Figure 13. In each panel, the histogram at the bottom is a fold of the entire observation. The smooth curve is obtained from the best-fit 5 harmonics. The histogram at the top is the long-term average. The first, second, and fourth folded profiles have a different shape from the long-term average; they occured during flares. Note how the first three bursts occur near the peak of the profile (burst phases 0.58±0.02, 0.64±0.02, and 0.66±0.02 relative to the template shown in the Figure), but the last burst is further from the peak (burst phase 0.43±0.02 relative to the template shown in the Figure).

7. Discussion

7.1. Pulsed Flux Variations

The goal of continued systematic *RXTE* monitoring of AXPs is to flesh out the phenomenological phase space of these intriguing objects. In this regard, 1E 1048.1−5937 has not disappointed us. It has shown a surprisingly diverse range of behaviors in practically every observational property. This includes its rotational evolution, in which we have seen several different timing anomalies – with two likely spin-up glitches – in addition to remarkable timing "noise", for lack of a better term. Its radiative evolution has been equally eventful, with 3 large, long-lived pulsed flux increases and multiple bursting episodes, as well as spectral changes and pulse profile changes. Understanding the physical origin of all this behavior is clearly very challenging; likely the best physical insights will come from considering multiple studies such as ours, for many different objects. Nevertheless here we consider what these phenomena may be telling us about the physics of magnetars.

Several AXPs have exhibited pulsed flux variations on long timescales. RXS J170849.0−400910 exhibited low-level pulsed flux variations on timescales of weeks to months (Dib et al. 2008). 4U 0142+61 exhibited a pulsed flux increase by 29±8% over a period of 2.6 years (Dib et al. 2007a). 1E 2259+586 exhibited an abrupt increase in the pulsed (and persistent) flux which decayed on timescales of months to years (Woods et al. 2004). This abrupt increase occured in conjunction with bursts, and the decay is thought to be due either to thermal radiation from the stellar surface after the deposition of heat from bursts (eg. Lyubarsky et al. 2002), or

the result of the slow decay of a magnetospheric "twist" (Thompson et al. 2002). This outburst was accompanied by a glitch. XTE 1810−197 and candidate AXP AX J1845−0258 also exhibited an increase in the pulsed flux although the risetime is unclear (Ibrahim et al. 2004; Torii et al. 1998; Tam et al. 2006).

The long-term pulsed flux behavior of AXP 1E 1048.1−5937 is different from that of any other AXP: in the first two flares exhibited by 1E 1048.1−5937, the pulsed flux rose on week-long timescales and subsequently decayed back on time scales of months to years (Gavriil & Kaspi 2004). It is unclear whether the third flare had a resolved rise (see Section 5). Although small bursts sometimes occured during these events (see Section 6), the afterglow of these small bursts cannot explain the overall flux enhancement, and in the absence of evidence for large bursts prior to the flare, we can attribute the flares to twists implanted in the external magnetosphere from stresses on the crust imposed by the internal magnetic field.

Based on the idea that a plasma corona is contained within the closed magnetosphere, Beloborodov & Thompson (2007) offer a prediction for the behavior of the luminosity of the source after a magnetospheric twist occurs. Assuming that a large flux enhancement is caused by a twist, that the emission from the heated crust is small compared to the magnetospheric emission of twisted magnetic flux tubes, and assuming no additional twists introduced after the original twist, Equation 17 of Beloborodov & Thompson (2007) predicts that the luminosity will decay linearly, and is proportional to $-\phi^2 \times (t - t_0)$, where ϕ is the voltage between two footpoints of a magnetic field line and $(t - t_0)$ is the time since the start of the decay of the luminosity. ϕ is induced by the current that accompanied the gradual untwisting of the magnetic field. Its minimum value is that needed for the creation of electron positron pairs. It is proportional to the local magnetic field.

Using Equation 3 and our pulsed flux time series, we produced a total flux time series for 1E 1048.1−5937 (Figure 14). We then fit a linear decay to the first few months of data after each of the three flares. Including data beyond that would have made the fits worse, indicating that we can attribute at most the first part of the decay to a linear twist relaxation. The second part could perhaps be attributed to crust afterglow following some internal heat deposition (see Section 7.3). The slopes of the linear fits had the values $-0.23(3)\times10^{-12}$ erg/s/cm^2/day, $-0.164(13)\times10^{-12}$ erg/s/cm^2/day, and $-0.083(5)\times10^{-12}$ erg/s/cm^2/day, with reduced χ^2 values of 0.72, 0.38, and 0.91, respectively. The fits were good, as predicted by Beloborodov & Thompson (2007), but the three slopes significantly differed from each other, suggesting, in the context of this model, that different flux tubes (with different values of local magnetic fields) were twisted in each event.

7.2. Timing Behavior

In addition to flux variability, regularly monitored AXPs also exhibit different kinds of timing variability. In RXS J170849.0−400910, the frequency derivative fluctuates by ∼8% about its long-term average ∼1.58 $\times10^{-13}$ s^{-2} on a timescale of months (Dib et al. 2009a), except at the second detected glitch which had an exponential recovery (Kaspi & Gavriil 2003). The frequency derivative of 1E 1841−045 varies by ∼10% on a timescale of many years, except at the first detected glitch where $\dot{\nu}$ suddenly dropped by ∼10% (Dib et al. 2008). It slowly dropped further before slowly recovering. The frequency derivative of 4U 0142+61 also fluctuates by ∼3% around its long-term average on a timescale of months to years, except at the onset of the 2007 active phase where it suddenly dropped (Gavriil et al. 2009b). It then slowly recovered. The frequency derivative of 1E 2259+586 also fluctuates about its long-term average, except at the first detected glitch, which had an exponential recovery (Woods et al. 2004).

The episode of extreme variations in $\dot{\nu}$ of 1E 1048.1−5937 is not seen in any other AXP. In 2002 and 2003, $\dot{\nu}$ varied by $\sim5.6\times10^{-13}$ s^{-2} every two weeks (time between consecutive sets of three observations), oscillating between -26×10^{-13} s^{-2} and -6×10^{-13} s^{-2} 4 times in the span of 450 days.

When trying to understand the origin of these variations, it is useful to look for correlation between the timing properties and the flux of the pulsar. Figure 15 is a plot of the timing and radiative behaviors of 1E 1048.1−5937.

Earlier we suggested that the flux variations in 1E 1048.1−5937 may be due to twists implanted

in the external magnetosphere from stresses on the crust imposed by the internal magnetic field. In the magnetar model, the twisting drives currents into the magnetosphere. The persistent non-thermal emission of AXPs is explained in this model as being generated by these currents through magnetospheric Comptonization (Thompson et al. 2002). Changes in X-ray luminosity, spectral hardness, pulse profile, and torque changes have a common origin in this model.

Gavriil & Kaspi (2004) looked for correlations between the $\dot{\nu}$ and the pulsed flux near the first two flares and reported only a marginal correlation. They suggested that the lack of correlation was because the torque is most sensitive to the current flowing on a relatively narrow bundle of field lines anchored close to the magnetic poles (Thompson et al. 2002). Therefore, whether an X-ray luminosity change will be accompanied by a $\dot{\nu}$ change depends on where in relation to the magnetic pole the source of enhanced X-rays is.

Earlier we suggested that the different decay slopes of the three different flares might indicate that different flux tubes, with different values of local magnetic field, were twisted in each event (Beloborodov & Thompson 2007). Therefore, even if there was no correlation between $\dot{\nu}$ and the pulsed flux in the case of the early flares, if the flux tubes involved in the third flare were closer to the poles, one might expect a correlation to occur in that flare. From Figure 15, this does not appear to be the case. Note that correlations between the luminosity and torque are also expected in accreting scenarios, and are not observed here.

An interesting observation is that episodes of rapid $\dot{\nu}$ variations appear to follow the second and third flares (see Section 5). Bi-monthly variations in $\dot{\nu}$ changed from 0.08×10^{-13} s^{-2} near the second flare to 2×10^{-13} s^{-2} 41 days after the same flare, to 5.6×10^{-13} s^{-2} 141 days after the flare. Similarly, weekly variations in $\dot{\nu}$ changed from 0.33×10^{-13} s^{-2} near the third flare to 0.6×10^{-13} s^{-2} 350 days after the flare, to 1.4×10^{-13} s^{-2} 395 days after the flare. This might only be a coincidence, however Beloborodov & Thompson (2007) predict that the impact of a twist in the magnetosphere on the spin-down may appear with a delay of $\sim$2 years. This is because the timescale of the twist spreading to the light cylinder is large due to the resistivity to the currents of the corona contained within the closed magnetosphere.

7.3. Glitches

In many glitch models, the superfluid in the crust is spinning faster than the crust, but on average over long times, they have the same $\dot{\nu}$. The superfluid cannot spin down because its angular momentum vortices are pinned to crustal nuclei and hence cannot move outward (see, for example, Alpar et al. 1989). For various reasons, for example, torques on the crust, internal starquakes and thermal agitations, unpinning of the vortex lines may happen in some locations. The vortices could then move outward, and the superfluid angular frequency can decrease and approach that of the crust. At that moment, angular momentum is transferred from the superfluid to the crust, and a glitch occurs. For example, Link & Epstein (1996) argued that starquakes due to magnetic stresses at the core/crust boundary in normal rotation-powered pulsars could deposit energy that then results in sudden spin-ups; such events seem even likelier to occur in magnetars, consistent with their ubiquitous glitching (Kaspi et al. 2000; Kaspi & Gavriil 2003; Dall'Osso et al. 2003; Dib et al. 2008; Israel et al. 2007).

The glitch coincident with the third pulsed flux flare of 1E 1048.1−5937 is the largest yet seen in the five regularly monitored AXPs, and has one of the largest fractional frequency increases in any pulsar, including rotation-powered sources. This event was not accompanied by a significant change in $\dot{\nu}$. In fact, in the months preceding the glitch, $\dot{\nu}$ became more and more negative, until three weeks prior to the glitch, when it started decreasing in magnitude, reaching a value not far from the one it adopted after the glitch. It is unclear if this behavior is somehow related to glitch; perhaps it caused the unpinning of the vortices. Unfortunately, the relation between what is usually considered to be timing noise and the behavior of the superfluid inside is not well understood.

What is clear, however, is that this glitch was associated with a radiative event: the third pulsed (and persistent) flux flare. Above, we suggested this flare may be due to a twist in the magnetosphere. The twist originates in a tangle of field lines below the surface of the star. Because of the

internal magnetic stresses inside, a piece of crust above the tangle is twisted, twisting the footpoints of the external magnetic field. Eventually this twist propagates outward. It is possible that some vortices that are pinned to the crust get mechanically dislodged when the crust is being twisted, causing a glitch, or that energy deposition during this event raises the temperature such that pinning is affected, as in the Link & Epstein (1996) picture.

In fact, we note that every observed AXP flare or outburst thus far has been accompanied by a timing event. In the case of 1E 2259+586 and the third flare of 1E 1048.1−5937, the event was a glitch (Woods et al. 2004, and Section 3.4). For 4U 0142+61 and for the second flare of 1E 1048.1−5937, the event was a sudden change in $\dot{\nu}$ possibly accompanied by a glitch (Gavriil et al. 2009b and Section 3.3). For the first flare of 1E 1048.1−5937 the event was a timing anomaly of uncertain nature (Section 3.2). It is possible that all these timing events were caused by some unpinning of superfluid vortices, which in turn was caused by crustal movement due to a twist propagating outward.

Note however that the converse is not true: many AXP glitches appear to be radiatively silent, such as the second glitch observed from 1E 2259+586, and all 4 glitches of AXP 1E 1841−045 (Dib et al. 2008, Dib et al. 2009a). There is no evidence of pulsed flux changes associated with the glitches of RXS J170849.0−400910, however there are claims of an association between variations in the total flux of the source and the glitch epochs (see, for example, Campana et al. 2007 and Israel et al. 2007). Why do we not see any released energy in the case of the "silent" glitches? Perhaps it is released deep in the star and some, or all, of it goes into the core. Perhaps when some energy reaches the surface, the delay between the energy release and the start of the associated increase in flux as well as the actual risetime of that increase are related to how deep below the surface this energy was released (see, for example, Cumming & Macbeth 2004, Brown & Cumming 2009). Since the risetime of the flux events associated with the "loud" glitches is never longer than a few months, one could speculate that any energy release that would have caused a larger risetime goes directly into the core.

Indeed, perhaps the radiative events accompanying some glitches are not due to a twist of the footpoints of the external field following crustal cracking. Perhaps the sudden unresolved increases in the flux, like that seen in the 2002 event from 1E 2259+586, are due to a twist propagating from the inside by breaking the crust (possibly combined with a thermal energy release due to the glitch), while the slow resolved increases in the flux, like those seen in the first two flares of 1E 1048.1−5937, are due to a local thermal energy release following a glitch.

7.4. Pulse Profile Changes

In Section 4, we showed that the largest pulse profile changes happen near the flares. In 1E 1048.1−5937, these changes always involve an increase in the harmonic content of the profiles. This suggests that these changes are not due to a surface disturbance (hot spot), since the effects of this on the profile would probably be smeared due to general relativistic light bending (Dedeo et al. 2001). Instead, they may be due to a local event in the magnetosphere.

Beloborodov & Thompson (2007) argued that it might take several years for the twist to propagate from the surface of the star to the light cylinder. Once the twist reaches the light cylinder, the torque affects the star almost immediately, and variations in $\dot{\nu}$ are observed. In this picture, early on, the twist is in the lower magnetosphere, and much later it is in the upper magnetosphere. A twist in the lower magnetosphere where the fields are very strong affects the properties of the local plasma, modifying its emission as well as the emission that is scattered from the surface below. In this case one might expect noticeable pulse profile changes. A twist that has reached the light cylinder where the fields are weaker affects the properties of the local plasma less, and affects the emission from the lower magnetosphere less. In this case one might expect the pulse profile changes to be much smaller. Thus, that we are seeing the pulse profile changes only at the beginning of the flares is consistent with the picture in Beloborodov & Thompson (2007).

If significant pulse profile changes *had* been observed at the time of the large $\dot{\nu}$ variations, this could have meant that the pulsed flux flares and the subsequent large $\dot{\nu}$ variations are independent.

In this case, the $\dot{\nu}$ changes would be due either to a low magnetospheric twist (accompanied by pulse profile changes) which propagates quickly to the light cylinder, causing the torque changes; but why the onset of this twist would not be accompanied by a visible energy release is unclear. Alternatively, the $\dot{\nu}$ changes may not be due to torques at the light cylinder, but to internal events which cause the crust to crack and the lower magnetosphere to twist itself. In this case too it would be unclear why no bursting activity or energy release was seen, and the unobserved pulse profile changes would be puzzling.

7.5. Long-Term Spectral Changes

In Section 5 we show that the hardness ratio of 1E 1048.1−5937, obtained from the pulsed flux, dropped significantly 9 months after the peak of the second flare, while the pulsed flux was still decaying, and while the large $\dot{\nu}$ variations were ongoing. Unfortunately, there are no imaging observations of the source around that time, and we cannot verify if the drop in the pulsed hardness ratio was accompanied by a drop in the hardness ratio of the persistent emission. Assuming that it was, this softening may be related to the magnetospheric twist that caused the flares. Indeed in the Thompson et al. (2002) model, spectral hardness is correlated with the luminosity. The hardness ratio is expected to gradually drop when the flux decays. However, the decrease seen here was sudden, not gradual. Also, this does not explain why the hardness ratio was not lower prior to the onset of the flares. Alternatively, this correlation of the softening with the flux decay can also be a consequence of changes in the effective temperatures of the outer layers of the star (Özel & Güver 2007), and the twisted magnetosphere model need not be invoked here.

7.6. Bursts

1E 1048.1−5937 is more active than the other AXPs we monitor in multiple regards. With *RXTE* monitoring over the past ∼10 years, it is the only one which exhibited three large flux flares, it is the only AXP which exhibited extreme variations in $\dot{\nu}$, and the glitch observed in conjunction with the third flare is the largest observed among these AXPs. In addition, 1E 1048.1−5937 has shown four bursts, at different epochs. Other AXPs, such as RXS J170849.0−400910 and 1E 1841−045, have shown none, even though the combined *RXTE* on-source time of these two sources is the same as that of 1E 1048.1−5937.

Since three of the observed bursts were followed by an enhancement in the 4−10 keV pulsed flux, it is possible that the high pulsed flux of the observation taken on 2005 November 08 (see Section 5) was due to a burst that occured just before the observation. We detected no evidence for a change in pulsed flux during this observation. Since it was the first in the weekly set of three closely spaced observations, the decay timescale of the putative burst could be such that the decay is not noticeable within the observation, given the size of our pulsed flux uncertainties. The observation that followed this one occured 18 hours later and its pulsed flux was consistent with the long-term average. We verified that there were no *SWIFT* triggers from the location of 1E 1048.1−5937 in the week preceding the anomalous observation.

The four bursts observed from 1E 1048.1−5937 were associated with different flaring events. Bursts 1 and 2 occured near the peak of the first flare. Burst 3 occured two years after the peak of the second flare, while the pulsed flux was still decaying. Burst 4 occured a month after the peak of the third flare. Bursts 1, 2, and 3 occured near pulse maximum. All four bursts had millisecond risetimes. Bursts 1, 3, and 4, had long decay tails (51 s, $>$ 700 s, and 128 s), with a pulsed flux enhancement in the tails. The falltime for burst 2 was 2 s. An apparent feature near 13 keV has been observed in the spectra of the first, and third bursts (Gavriil et al. 2002, 2004), and an apparent feature near 15 keV has been observed in the spectrum of the most recent burst. Note that apparent features near 13 keV have also been observed in the tail of one of the bursts in AXP XTE J1810−197 (Woods et al. 2005), and in the spectrum of the largest burst detected in AXP 4U 0142+61 (Gavriil et al. 2009b). So far the presence of these features is not well understood.

Woods et al. (2005) suggest that there are two types of magnetar bursts. Type A bursts are short, symmetric, and occur uniformly in pulse phase. Type B bursts have long tails, thermal spectra, and occur preferentially at pulse maximum. They also noted that Type B bursts occur preferentially

in AXPs (although AXP 1E 2259+586 emitted both kinds of bursts during its 2002 outburst), and Type A bursts occur primarily in SGRs.

Woods et al. (2005) argue that type A bursts are due to reconnections in the upper magnetosphere, and that type B bursts are due to crustal fracture followed by a rearrangement of the magnetic field lines outside the surface. They explain that a magnetospheric origin would lend itself to more isotropic emission having no preference for a particular pulse phase, while the crust fracture model would naturally produce a phase dependence of the burst emission for a localized active region on the crust. The tendency of the bursts to occur near pulse maximum is consistent with the strain in the crust causing the cracking being highest in the regions where the field is the strongest: at the polar caps. Furthermore, Thompson et al. (2002) have argued that the SGRs, with their strong non-thermal spectral components, undergo more reconnection events. Therefore, if the type A bursts are really due to magnetospheric events, then it makes sense that they occur more in SGRs.

None of the bursts observed from 1E 1048.1−5937 is of the symmetric type. All four bursts had a long tail with pulsed flux enhancement, except in burst 2 where the tail was very short, but still $\sim$ 300 times longer than the risetime. Therefore all four are probably bursts of Type B. However, burst 4 did not occur near pulse maximum. This does not necessarily mean that the above interpretation of Types A and B bursts is wrong; rather, for this burst, perhaps the crustal cracking did not occur near the polar cap, or near the hot spot that usually yields the pulse.

Note that a similar situation occured for AXP 4U 0142+61. Six bursts were detected from this AXP during the 2006 active phase (Gavriil et al. 2009b). None of them was a short and symmetric Type A burst: they all had tails, although in two cases the tails were shorter than 10 s. Burst 1 occured at pulse maximum. Bursts 2 to 5 all occured within a single observation, and two of them did not occur near pulse maximum. Presumably some global event had caused the crust to crack at many places. Not only did burst 6 not occur at pulse maximum, but it occured where a temporary new peak in the profile appeared. Here, just like for burst 4 of 1E 1048.1−5937, a large crack could have appeared away from the usual location of the emission.

8. Summary

We have presented a long-term study of the timing properties, the pulsed flux, and the pulse profile of AXP 1E 1048.1−5937 as measured by *RXTE* from 1996 to 2008. We showed that the onset of the 2001 pulsed flux flare was accompanied by a timing anomaly and by significant pulse profile changes. The timing anomaly was consistent with a gradual slow down lasting 2−3 weeks followed by a recovery. We showed that the onset of the 2002 pulsed flux flare was accompanied by a likely glitch of size $\Delta\nu/\nu = 2.91(9) \times 10^{-6}$, by a large change in $\dot{\nu} = -4.10(14) \times 10^{-14}$, and by significant pulse profile changes. We use the term "likely" because, while the trend in the timing residuals indicates that a glitch occured, due to the finite resolution of the data, which is particularly problematic given the extreme timing noise of this source, a rapid non-instantaneous variation cannot be ruled out. Both of these flares had few-weeks-long risetime. Several months after the peak of the second flare, and while the pulsed flux was still decaying, the source underwent extreme $\dot{\nu}$ variations lasting $\sim$450 days. Then the source entered a period of relative timing quiescence in which no radiative changes were observed except for occasional low-level pulse profile changes. The source reactivated in 2007 and a third pulsed flux flare was observed. The risetime of that flare was < 7.3 days. It is unclear whether the rise was resolved. Contemporaneous imaging observations showed that the persistent flux rose also. The onset of this flare was accompanied by a very large spin-up glitch ($\Delta\nu/\nu = 1.63(2) \times 10^{-5}$) and by many significant but short-lived pulse profile changes. In total, four short non-symmetric bursts have been observed in this source to date.

The three pulsed flux flares can be attributed to twists implanted in the external magnetosphere from stresses on the crust imposed by the internal magnetic field. Beloborodov & Thompson (2007) postulated the presence of a plasma corona within the closed magnetosphere and predicted a linear decay in the flux following the initial rise due to the twist. The first part of the decay of the observed flares can be well fit with a linear trend, but not the entire decay. Alternatively, the flares

can be attributed to an internal heat release associated with the contemporaneous timing events, although the pulse profile changes seen contemporaneously with the flares likely have a magnetospheric origin. All three flares were accompanied by either a timing anomaly or a glitch. This can be due to a disturbance in the superfluid vortex lines caused by the crustal disturbance at the time the twist was implanted. The extreme timing noise observed several months after the peak of the second flare may be attributed, in the Beloborodov & Thompson (2007) picture, to the twist associated with the flare finally having reached the light cylinder, although it is hard to understand the magnitude and the timescale of the variability in this picture. Finally, all four bursts observed in this source can be attributed to the crustal cracking that occured when the twist propagated from the inside of the star to the lower magnetosphere.

A coherent physical picture explaining the variety of behaviors observed in this fascinating source, as well as in other AXPs, has yet to emerge, however we hope through continued detailed studies such as the one presented here, one will be forthcoming soon. Thus far, the framework of the magnetar model appears most promising to us.

We thank A. Cumming and D. Eichler for useful discussions. Support was provided to VMK by NSERC Discovery Grant Rgpin 228738-08, an FQRNT Centre Grant, CIFAR, the Canada Research Chairs Program and the Lorne Trottier Chair in Astrophysics and Cosmology.

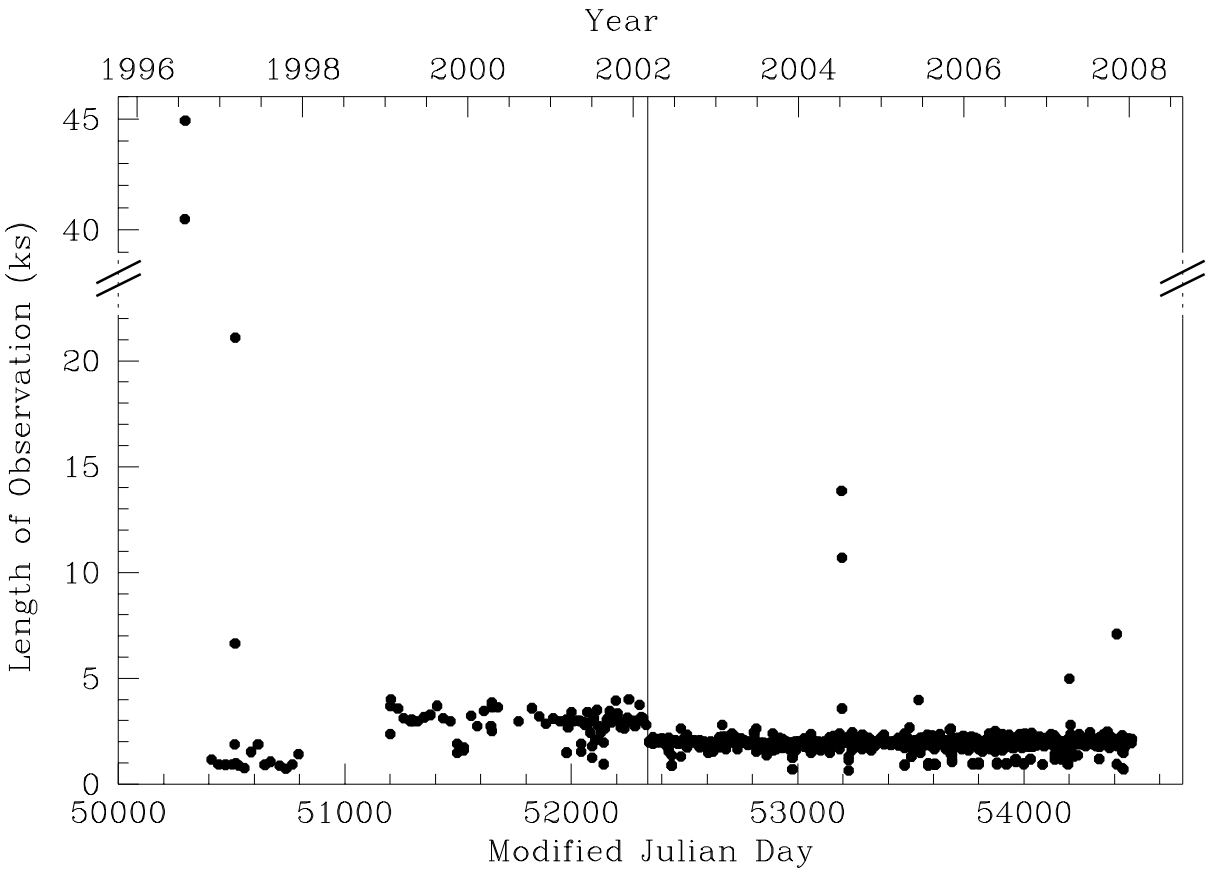

Fig. 1.— Length (on-source integration time) of the *RXTE* observations of 1E 1048.1−5937 used in this paper versus epoch. The solid line indicates when we adopted the strategy of observing the source with sets of three closely spaced observations.

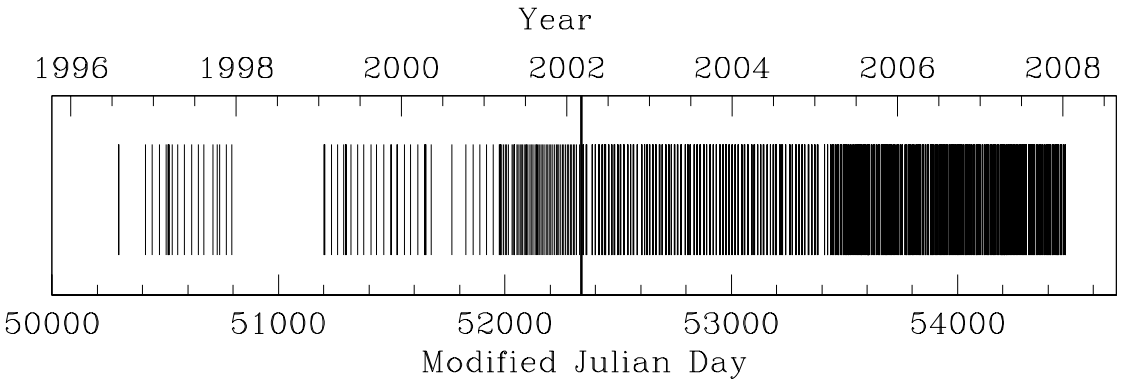

Fig. 2.— Epochs of the observations of 1E 1048.1−5937 used in this paper. The bold line indicates when we adopted the strategy of observing the source with sets of three closely spaced observations.

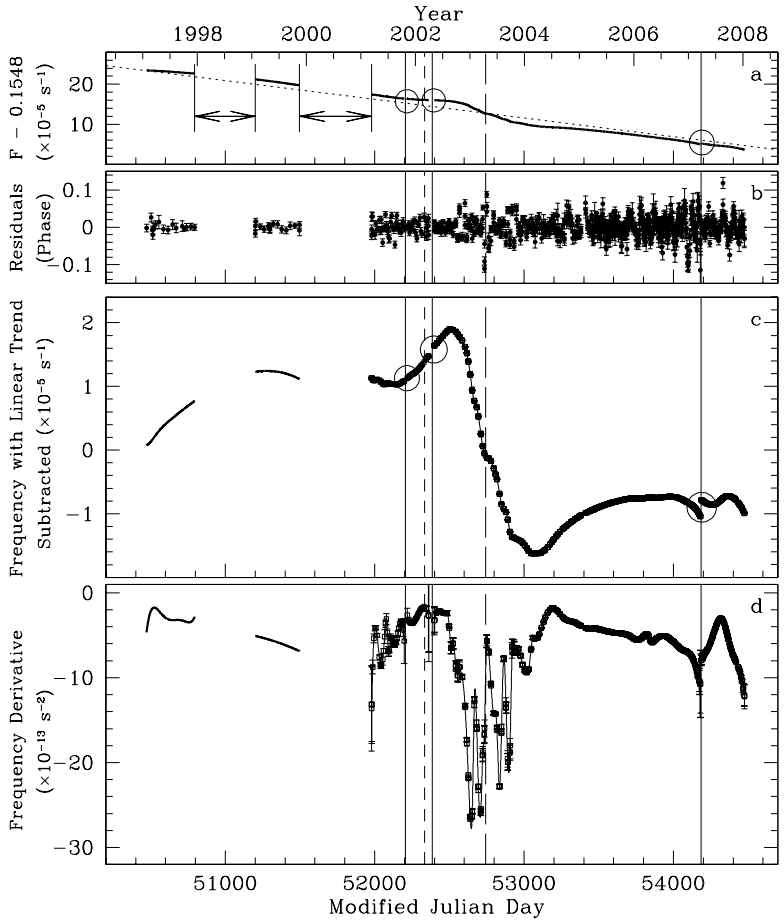

Fig. 3.— Timing properties of AXP 1E 1048.1−5937. (*a*) Long-term evolution of the frequency of 1E 1048.1−5937. The slope of the diagonal dotted line is the average spin-down of the pulsar ($\sim -5.4 \times 10^{-13}$ s^{-2}). The deviations from the average spin-down are clear to the eye. The three circles are centered at the start of the three pulsed flux flares (see Figures 10 and 15), and mark the location of a timing anomaly, a likely glitch, and a glitch. (*b*) Timing residuals obtained after subtracting the TOAs from the ephemerides plotted in panel a. (*c*) Long-term frequency evolution with the long-term average spin-down subtracted. For the first two plotted curves, the error bars are smaller than the width of the lines. The three circles are centered at the start of the three pulsed flux flares, and mark the location of a timing anomaly and two glitches (see Sections 3.2−3.4 in the text). (*d*) Long-term evolution of the frequency derivative of the pulsar. *All panels:* The three solid lines indicate the onset of the three pulsed flux flares. The short-dashed line marks the epoch when we started observing the source in sets of three closely spaced observations. The long-dashed line indicates the epoch when the overlap in the partial ephemerides was for a single set of three observations (see Section 3.1 for details).

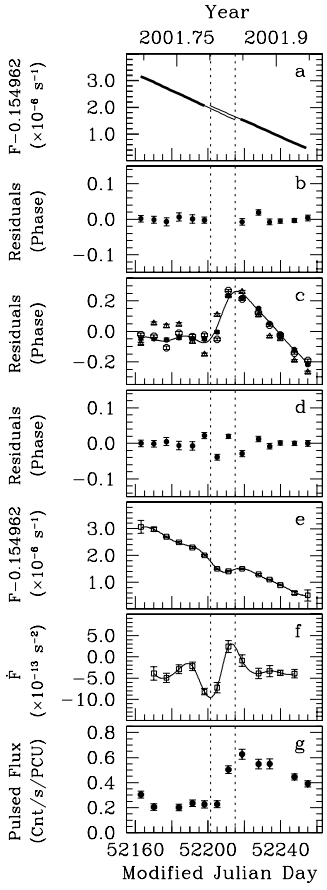

Fig. 4.— Timing properties of AXP 1E 1048.1−5937 near the onset of the first flare (MJD 52254 − 52163). The two dotted lines enclose the data from the week preceding and following the onset of the flare. (*a*) Frequency versus time, showing the TEMPO-obtained pre-flare and post-flare ephemerides, not including the data points between the dotted lines. The lines shown between the double dotted lines are extentions of the pre-flare and the post-flare ephemerides. (*b*) Timing residuals corresponding to panel a. (*c*) Data points: timing residuals for three different sets of TOAs obtained after subtracting the TOAs from the pre-flare ephemeris (see Section 3.2 for details). Solid curve: the spline that best fit the pre-flare and post-flare TOAs subtracted from the pre-flare ephemeris. (*d*) Timing residuals obtained after subtracting the original TOAs from the spline. (*e*) Frequency obtained by evaluating the derivative of the spline shown in panel c. (*f*) Frequency derivative obtained by evaluating the second derivative of the spline shown in panel c. (*g*) The 2−10 keV RMS pulsed flux of the pulsar near the onset of the first flare.

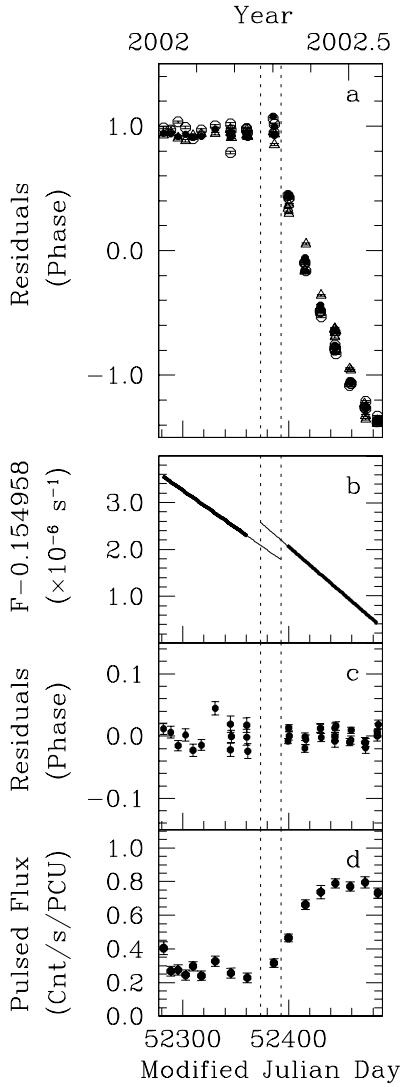

Fig. 5.— Timing properties of AXP 1E 1048.1−5937 near the onset of the second flare (MJD 52282 − 52485). The two dotted lines enclose the data from the week when the pulsed flux started rising. (*a*) Timing residuals for three different sets of TOAs obtained after subtracting the TOAs from the pre-flare ephemeris (see Section 3.3 for details). (*b*) Frequency versus time obtained from the original set of TOAs showing the `TEMPO`-obtained pre-flare and post-flare ephemerides, not including the data points between the dotted lines. (*c*) Timing residuals corresponding to panel b. (*d*) The 2−10 keV RMS pulsed flux of the pulsar near the onset of the second flare.

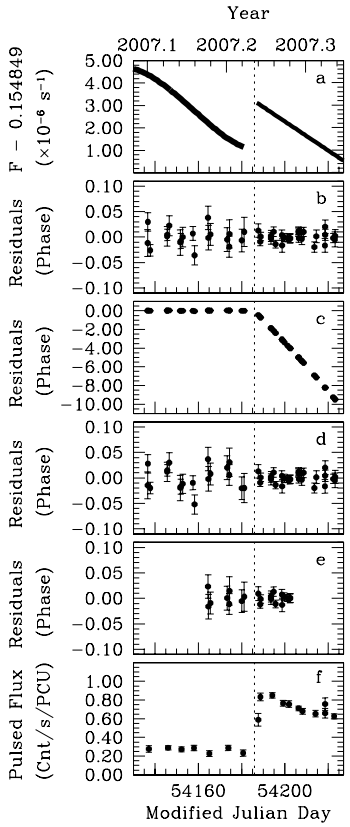

Fig. 6.— Timing properties of AXP 1E 1048.1−5937 near the onset of the third flare (MJD 54131 − 54223). The dotted line marks the epoch of a large glitch (see Section 3.4 for details). (*a*) Frequency versus time of the pre-flare and post-flare ephemerides. The pre-flare ephemeris consists of a frequency and three frequency derivatives. Notice how the curve is flatter in the two weeks preceding the flare. The post-flare ephemeris consists of a frequency and a single frequency derivative. (*b*) Timing residuals corresponding to panel a. (*c*) Residuals obtained after subtracting pre-flare and post-flare TOAs from a pre-flare ephemeris consisting of a frequency and frequency derivative. The change in the slope marks the occurence of the glitch. (*d*) Timing residuals obtained after fitting a glitch through the data for the 14 weeks surrounding the glitch. The RMS phase residual is 1.6%. (*e*) Timing residuals obtained after fitting a glitch through the data for the 6 weeks surrounding the glitch. The RMS phase residual is 0.98%. (*f*) The 2−10 keV RMS pulsed flux of the pulsar near the onset of the third flare (see Section 3.4 for details).

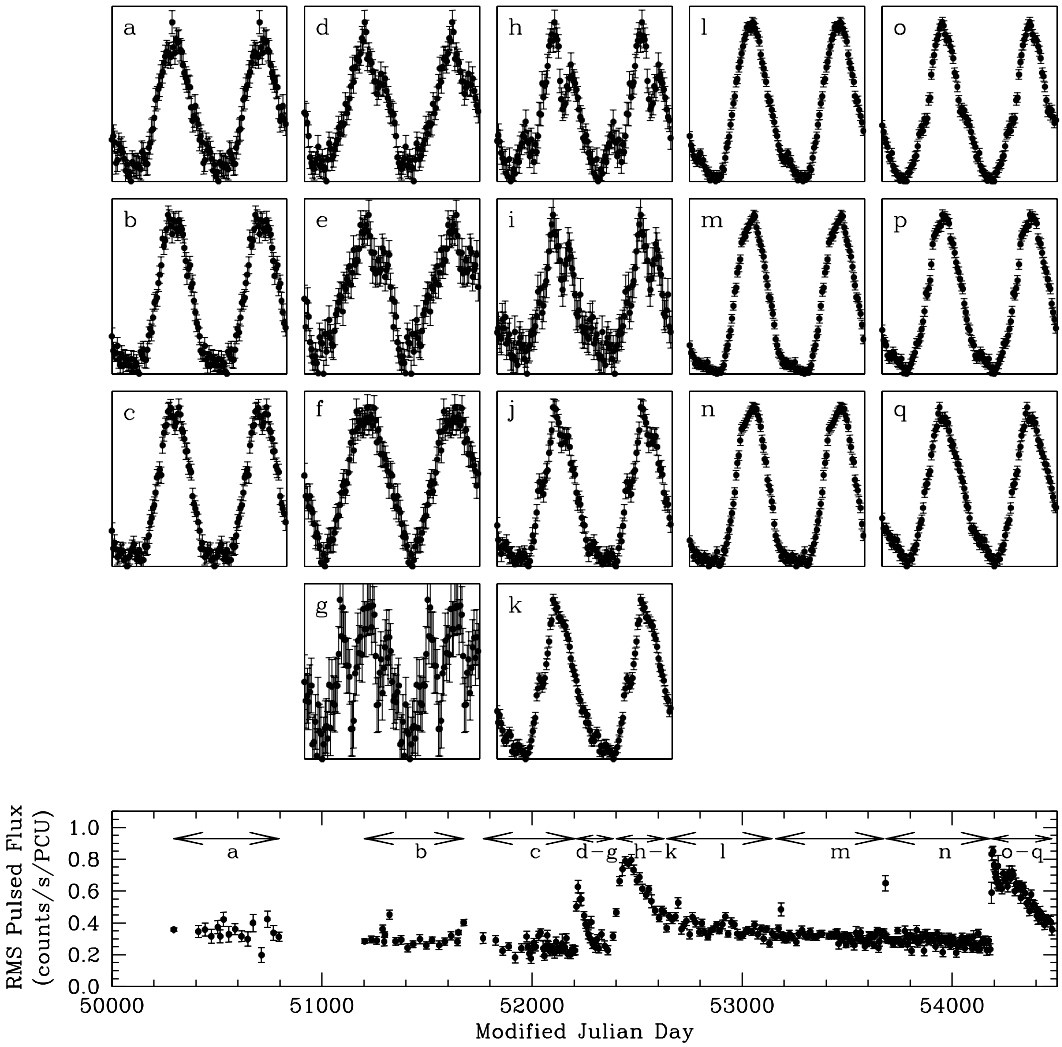

Fig. 7.— Normalized 2−10 keV pulse profiles of 1E 1048.1−5937 from 1997 to 2008. The letter shown in the top-left corner of each plot refers to the time segments marked by arrows in the bottom plot, where the 2−10 keV RMS pulsed flux is shown for reference.

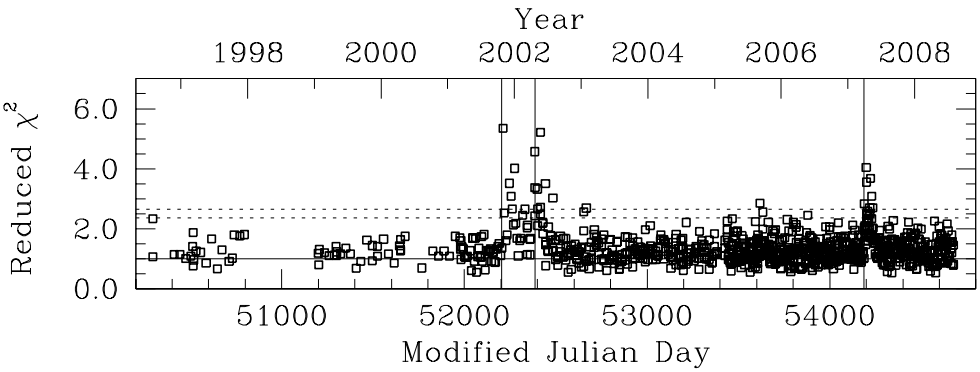

Fig. 8.— Reduced χ^2 statistics versus time, calculated after subtracting the scaled and aligned profiles of the individual observations from a high signal-to-noise template. The solid vertical lines indicate the onsets of the flares. The solid horizontal line indicates a reduced χ^2 of 1. The lower dotted line corresponds to the 2 σ significance level. The upper dotted line corresponds to the 3 σ significance level.

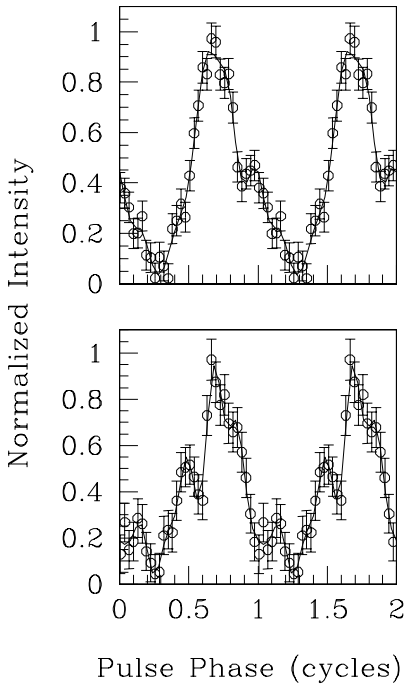

Fig. 9.— Normalized 2−10 keV pulse profiles from two observations taken during the decay of the third flare. The first observation was taken on 2007 April 09 (14 days after the glitch epoch). The second observation was taken on 2007 May 03 (38 days after the glitch epoch). The multiple peaks in the profile are obvious.

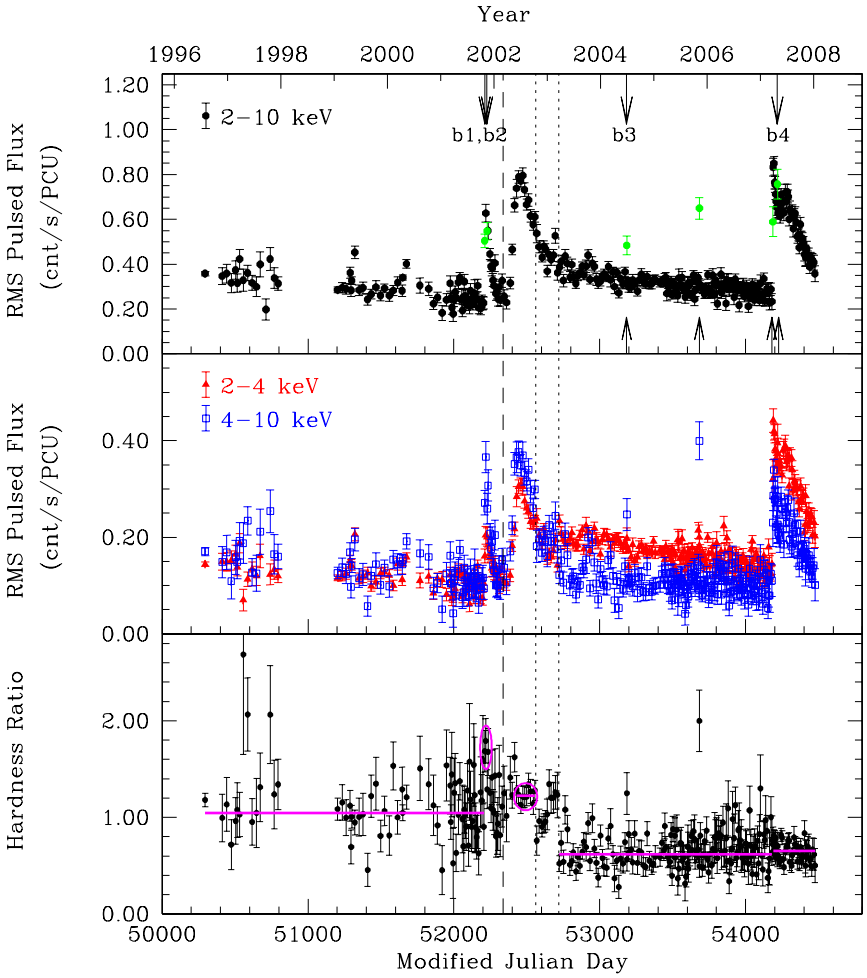

Fig. 10.— *Top:* Pulsed flux time series in the 2−10 keV band. For observations taken after 2002 March 02, we plotted the average of the pulsed flux values of each three closely spaced observations, with the 4 exceptions indicated by arrows along the bottom of the panel. All observations containing bursts are indicated by arrows along the top of the panel. All points indicated with an arrow are also coloured in green. *Middle:* Pulsed flux time series in the 2−4 keV band (red triangles) and in the 4−10 keV band (blue squares). *Bottom:* Hardness ratio computed from the pulsed flux in the energy range (4−10 keV)/(2−4 keV). The hardness ratios near the peaks of the first two flares are marked with two magenta circles. *All panels:* The dashed line indicates the epoch when we started observing the source with sets of three closely spaced observations. The left dotted line marks the location when the hardness ratio dropped, 342 days after the peak of the second flare. The right dotted line marks the location when the hardness ratio drops further, 500 days after the peak of the second flare.

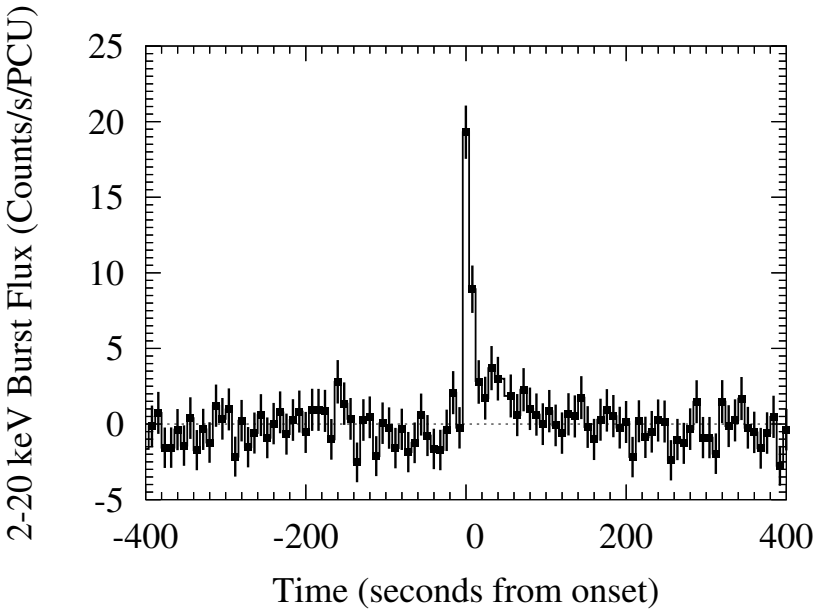

Fig. 11.— Background subtracted 2−20 keV burst light curve binned with 8 s time resolution.

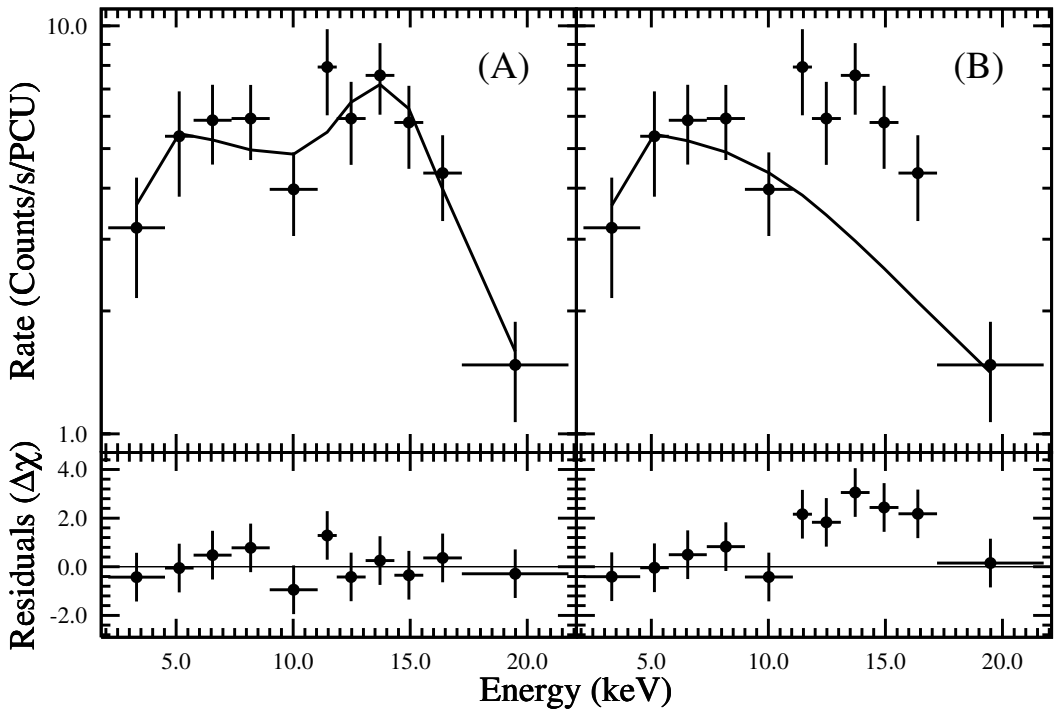

Fig. 12.— Spectral fits of the first 3 seconds of the new burst. (*a*) Photoelectrically absorbed power-law plus Gaussian model. (*b*) Photoelectrically absorbed power-law model.

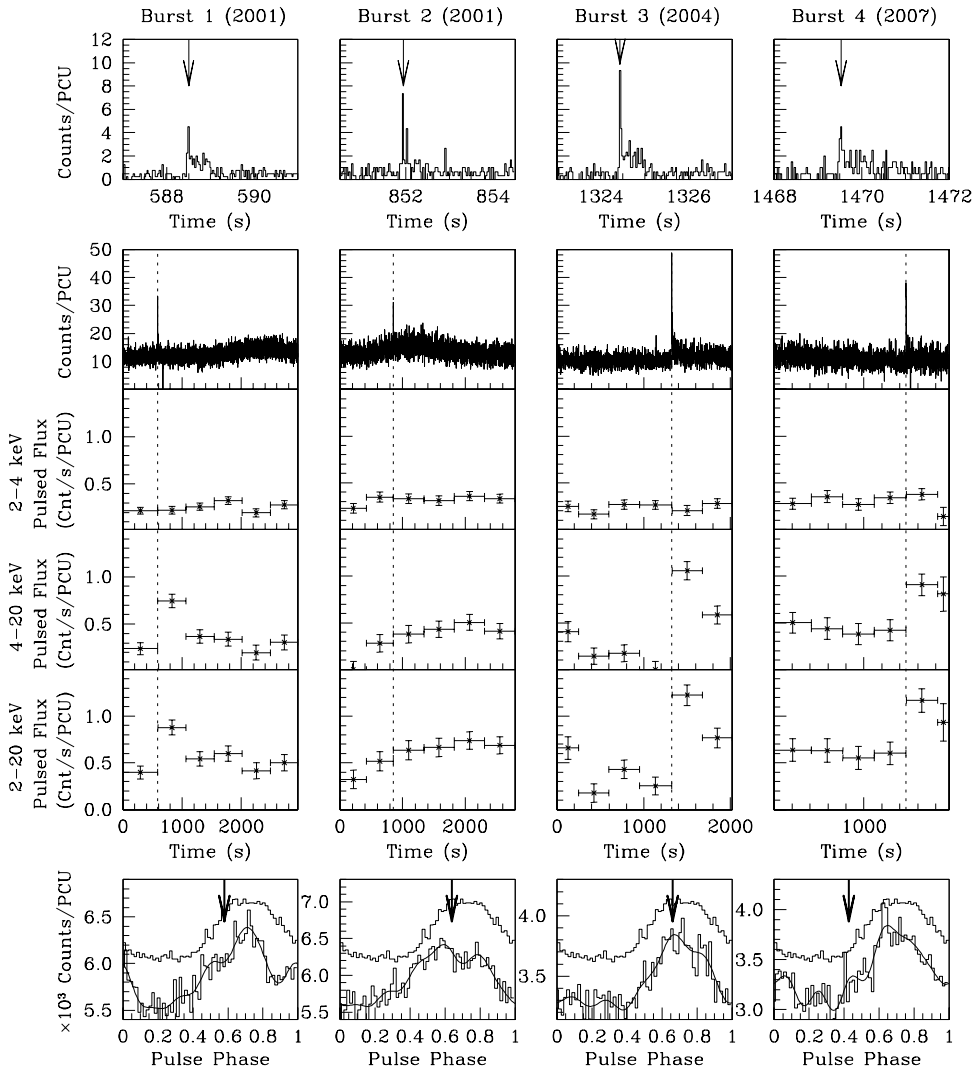

Fig. 13.— Short-term pulsed flux variability near the bursts, and burst phases. Each column corresponds to an observation in which a burst was detected. In each column: *Top:* a 4-s long time series with 31.25 ms time resolution showing the burst. The peak of the burst is indicated with an arrow. *Middle:* time series of the entire observation with 1-s time resolution, followed by the RMS pulsed flux in three different bands. We excluded the 4 s surrounding the burst for this pulsed flux analysis. *Bottom:* A fold of the entire observation shown below the scaled long-term average profile. The phase at which the burst occured is marked with an arrow. This phase corresponds to the time bin indicated with an arrow in the top plot.

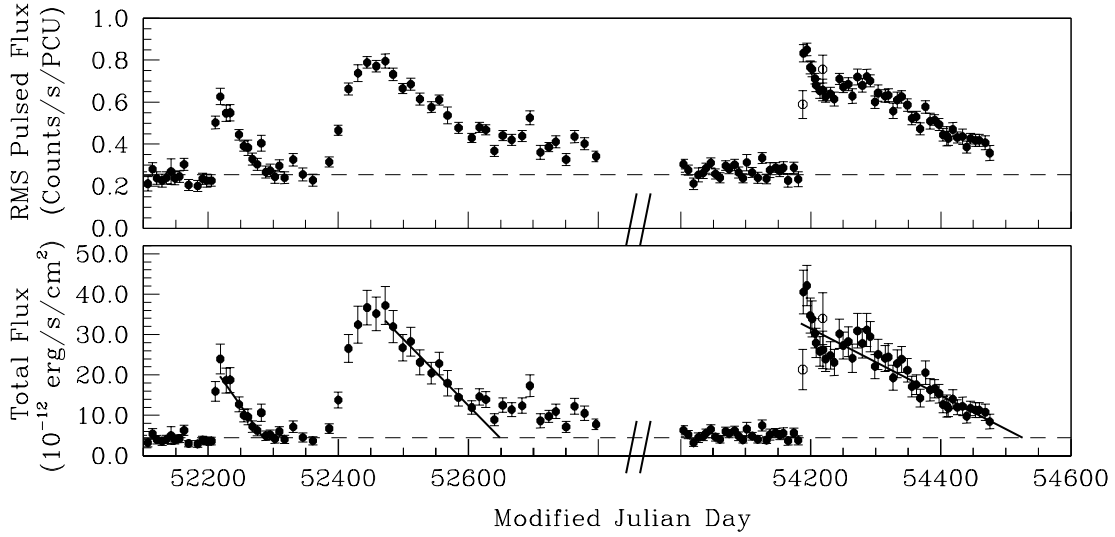

Fig. 14.— *Top:* Pulsed flux in the 2−10 keV near the three flares. *Bottom:* Simulated total 2−10 keV unabsorbed flux, estimated from the *RXTE* pulsed flux and from the power-law correlation between the pulsed fraction and the total flux described by Tam et al. (2008). The solid lines in the bottom plot are linear decays fit to the first few months of data after each of the flares.

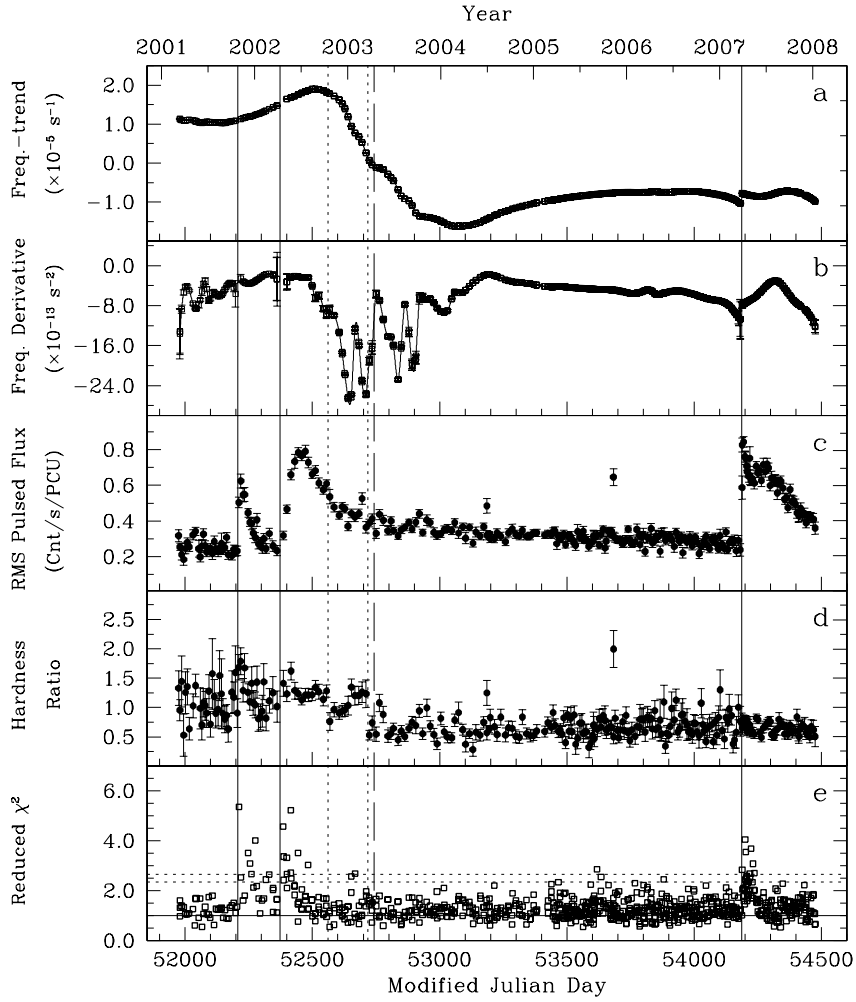

Fig. 15.— Evolution of the different properties of 1E 1048.1−5937. (*a*) Frequency as a function of time, with the long-term average spin-down subtracted. (*b*) The frequency derivative as a function of time. (*c*) The 2−10 keV RMS pulsed flux as a function of time. (*d*) The hardness ratio as a function of time, computed from the pulsed flux in the energy range (4−10 keV)/(2−4 keV). (*e*) Reduced χ^2 statistics as a function of time, calculated after subtracting the scaled and aligned profiles of the individual observations from a high signal-to-noise template. *All panels:* The three solid lines mark the onset of the three flares. The line with the long dashes marks the location where the ephemerides used to obtain the splines overlapped for a short period of time only. The two dotted lines mark epochs where the hardness ratio dropped, and maintained a lower value for the following weeks relative to the values preceding the drop.

TABLE 1
LOCAL EPHEMERIS OF 1E 1048.1−5937 NEAR THE 2007 GLITCH[a]

Parameter	Value
MJD range	54164.545−54202.475
TOAs	21
Epoch (MJD)	54185.912956
ν (s^{-1})	0.15484969(6)
$\dot{\nu}$ (s^{-2})	$-8.2(5)\times10^{-13}$
Glitch Epoch (MJD)	54185.912956
$\Delta\nu$ (s^{-1})	$2.52(3)\times10^{-6}$
$\Delta\dot{\nu}$ (s^{-2})	$6(4)\times10^{-14}$
RMS residual (phase)	0.0098

[a]Numbers in parentheses are TEMPO-reported 1σ uncertainties.

TABLE 2
BURST TIMING AND SPECTRAL PROPERTIES

Temporal Properties	
Burst day (MJD)	54218
Burst start time (fraction of day)	0.578621(6)
Burst rise time, t_r (ms)	955^{+80}_{-115}
Burst duration, T_{90} (s)	111.2^{+26}_{-19}
Fluxes and Fluences	
T_{90} fluence[a] (counts/PCU)	445±15
T_{90} fluence[a] ($\times 10^{-10}$ erg cm^{-2})	68.9±2.3
Peak flux for 64 ms[a] ($\times 10^{-10}$ erg s^{-1} cm^{-2})	24.2±5.4
Peak flux for t_r ms[a] ($\times 10^{-10}$ erg s^{-1} cm^{-2})	15.9±1.1
Spectral Properties	
Power law:	
Power law index	$0.37^{+0.20}_{-0.19}$
Unabsorbed power law flux ($\times 10^{-11}$ erg s^{-1} cm^{-2})	$4.64^{+0.44}_{-0.44}$
Reduced χ^2/degrees of freedom	1.80/18
Blackbody:	
kT (keV)	$4.9^{+0.7}_{-0.6}$
Unabsorbed Blackbody flux ($\times 10^{-11}$ erg s^{-1} cm^{-2})	$5.01^{+1.32}_{-1.34}$
Blackbody Radius[b] (km)	$0.014^{+0.006}_{-0.004}$
Reduced χ^2/degrees of freedom	1.20/18

[a]Fluxes and fluences are calculated in the 2–20 keV band.

[b]Assuming a distance of 9.0 kpc to the source (Durant & van Kerkwijk 2006).

TABLE 3
SPECTRAL FIT TO THE FIRST 3 SECONDS OF THE NEW BURST

Parameter	Value			
	Power-Law	Power-Law + Gaussian	Blackbody	Blackbody + Gaussian
Index/Temperature (keV)	$\sim$0.44	$0.71^{+0.28}_{-0.23}$	$6.12^{+0.80}_{-0.66}$	$5.26^{+0.99}_{-0.99}$
Continuum Flux[a]	$5.63^{+0.46}_{-2.65}$	$4.49^{+0.60}_{-0.68}$	$6.55^{+0.34}_{-0.77}$	$5.44^{+1.40}_{-1.24}$
Line Energy (keV)	...	$14.61^{+0.50}_{-0.52}$	...	$14.88^{+0.60}_{-0.57}$
Line Width (keV)	...	$1.81^{+0.73}_{-0.60}$	...	$1.35^{+0.68}_{-0.83}$
Line Flux[a] ($\times 10^{-10}$ erg s^{-1} cm^{-2})	...	$2.70^{+0.74}_{-0.79}$	...	$1.91^{+1.00}_{-0.75}$
Reduced χ^2/degrees of freedom	2.49/11	1.08/8	1.71/11	1.04/8

[a]Fluxes are unabsorbed and calculated in the 2–20 keV band, in units of $\times 10^{-10}$ erg s^{-1} cm^{-2}.

REFERENCES

Alpar, M. A., Cheng, K. S., & Pines, D. 1989, ApJ, 346, 823

Archibald, A. M., Dib, R., Livingstone, M. A., & Kaspi, V. M. 2008, in American Institute of Physics Conference Series, Vol. 983, 40 Years of Pulsars: Millisecond Pulsars, Magnetars and More, 265–267

Beloborodov, A. M. & Thompson, C. 2007, ApJ, 657, 967

Brown, E. & Cumming, A. 2009, ApJ, 698, 1020

Camilo, F., Ransom, S. M., Halpern, J. P., & Reynolds, J. 2007, ApJ, 666, L93

Campana, S., Rea, N., Israel, G. L., Turolla, R., & Zane, S. 2007, A&A, 463, 1047

Cumming, A. & Macbeth, J. 2004, ApJ, 603, L37

Dall'Osso, S., Israel, G. L., Stella, L., Possenti, A., & Perozzi, E. 2003, ApJ, 599, 485

Dedeo, S., Psaltis, D., & Narayan, R. 2001, ApJ, 559, 346

Dhillon, V. S., Marsh, T. R., Littlefair, S. P., Copperwheat, C. M., Kerry, P., Dib, R., Durant, M., Kaspi, V. M., Mignani, R. P., & Shearer, A. 2009, MNRAS, 394, L112

Dib, R., Gavriil, F. P., & Kaspi, V. M. 2009a, ApJ, in preparation

Dib, R., Kaspi, V. M., & Gavriil, F. P. 2007a, ApJ, 666, 1152

—. 2008, ApJ, 673, 1044

Dib, R., Kaspi, V. M., Gavriil, F. P., & Woods, P. M. 2007b, ATel, 1041

Dierckx, F. 1975, J. Comput. Appl. Math., 1, 165

Durant, M. & van Kerkwijk, M. H. 2006, ApJ, 650, 1070

Gaensler, B. M., McClure-Griffiths, N. M., Oey, M. S., Haverkorn, M., Dickey, J. M., & Green, A. J. 2005, ApJ, 620, L95

Gavriil, F. P., Dib, R., & Kaspi, V. M. 2009, ArXiv e-prints/0905.1256, submitted to ApJ

Gavriil, F. P. & Kaspi, V. M. 2004, ApJ, 609, L67

Gavriil, F. P., Kaspi, V. M., & Woods, P. M. 2002, Nature, 419, 142

—. 2004, ApJ, 607, 959

Gavriil, F. P., Kaspi, V. M., & Woods, P. M. 2006, ApJ, 641, 418

Gelfand, J. D. & Gaensler, B. M. 2007, ApJ, 667, 1111

Ibrahim, A. I., Markwardt, C. B., Swank, J. H., Ransom, S., Roberts, M., Kaspi, V., Woods, P. M., Safi-Harb, S., Balman, S., Parke, W. C., Kouveliotou, C., Hurley, K., & Cline, T. 2004, ApJ, 609, L21

Israel, G. L., Campana, S., Dall'Osso, S., Muno, M. P., Cummings, J., Perna, R., & Stella, L. 2007, ApJ, 664, 448

Israel, G. L., Covino, S., Stella, L., Campana, S., Marconi, G., Mereghetti, S., Mignani, R., Negueruela, I., Oosterbroek, T., Parmar, A. N., Burderi, L., & Angelini, L. 2002, ApJ, 580, L143

Israel, G. L., Götz, D., Zane, S., Dall'Osso, S., Rea, N., & Stella, L. 2007, A&A, 476, L9

Jahoda, K., Swank, J. H., Giles, A. B., Stark, M. J., Strohmayer, T., Zhang, W., & Morgan, E. H. 1996, Proc. SPIE, 2808, 59

Kaspi, V. M. 2007, Ap&SS, 308, 1

Kaspi, V. M. & Gavriil, F. P. 2003, ApJ, 596, L71

Kaspi, V. M., Gavriil, F. P., Chakrabarty, D., Lackey, J. R., & Muno, M. P. 2001, ApJ, 558, 253

Kaspi, V. M., Lackey, J. R., & Chakrabarty, D. 2000, ApJ, 537, L31

Link, B. & Epstein, R. I. 1996, ApJ, 457, 844

Lyubarsky, Y., Eichler, D., & Thompson, C. 2002, ApJ, 580, L69

Mereghetti, S. 2008, A&A Rev., 15, 225

Mereghetti, S., Tiengo, A., Stella, L., Israel, G. L., Rea, N., Zane, S., & Oosterbroek, T. 2004, ApJ, 608, 427

Özel, F. & Güver, T. 2007, ApJ, 659, L141

Tam, C. R., Gavriil, F. P., Dib, R., Kaspi, V. M., Woods, P. M., & Bassa, C. 2008, ApJ, 677, 503

Tam, C. R., Kaspi, V. M., Gaensler, B. M., & Gotthelf, E. V. 2006, ApJ, 652, 548

Thompson, C. & Duncan, R. C. 1995, MNRAS, 275, 255

Thompson, C. & Duncan, R. C. 1996, ApJ, 473, 322

Thompson, C., Lyutikov, M., & Kulkarni, S. R. 2002, ApJ, 574, 332

Tiengo, A., Mereghetti, S., Turolla, R., Zane, S., Rea, N., Stella, L., & Israel, G. L. 2005, A&A, 437, 997

Torii, K., Kinugasa, K., Katayama, K., Tsunemi, H., & Yamauchi, S. 1998, ApJ, 503, 843

Wang, Z., Bassa, C., Kaspi, V. M., Bryant, J. J., & Morrell, N. 2008, ApJ, 679, 1443

Wang, Z. & Chakrabarty, D. 2002, ApJ, 579, L33

Woods, P. M., Kaspi, V. M., Thompson, C., Gavriil, F. P., Marshall, H. L., Chakrabarty, D., Flanagan, K., Heyl, J., & Hernquist, L. 2004, ApJ, 605, 378

Woods, P. M., Kouveliotou, C., Gavriil, F. P., Kaspi, M., V., Roberts, M. S. E., Ibrahim, A., Markwardt, C. B., Swank, J. H., & Finger, M. H. 2005, ApJ, 629, 985

This 2-column preprint was prepared with the AAS LaTeX macros v5.2.